

# NGC628 with SITELLE : I. Imaging Spectroscopy of 4285 HII region candidates.

L. Rousseau-Nepton<sup>1,2,3\*</sup>, C. Robert<sup>2</sup>, L. Drissen<sup>2</sup>, R. P. Martin<sup>3</sup>,  
and T. Martin<sup>2</sup>

<sup>1</sup> *Canada-France-Hawaii Telescope, Kamuela, HI, 96743, USA*

<sup>2</sup> *Département de physique, de génie physique et d'optique, Université Laval, Québec, QC, G1V 0A6, CA*

*Centre de Recherche en Astrophysique du Québec*

<sup>3</sup> *Department of Physics and Astronomy, University of Hawaii at Hilo, Hilo, HI, 96720, USA*

Accepted XXX. Received XXX; in original form XXX

## ABSTRACT

This is the first paper of a series dedicated to nebular physics and the chemical evolution of nearby galaxies by investigating large samples of HII regions with the CFHT imaging spectrograph SITELLE. We present a technique adapted to imaging spectroscopy to identify and extract parameters from 4285 HII region candidates found in the disc of NGC 628. Using both the spatial and spectral capabilities of SITELLE, our technique enables the extraction of the position, dust extinction, velocity, H $\alpha$  profile, diffuse ionized gas (DIG) background, luminosity, size, morphological type, and the emission line fluxes for individual spaxels and the integrated spectrum for each region. We have produced a well-sampled HII region luminosity function and studied its variation with galactocentric radius and level of the DIG background. We found a slope  $\alpha$  of  $-1.12 \pm 0.03$  with no evidence of a break at high luminosity. Based on the width of the region profile, bright regions are rather compact, while faint regions are seen over a wide range of sizes. The radius function reveals a slope of  $-1.81 \pm 0.02$ . BPT diagrams of the individual spaxels and integrated line ratios confirm that most detections are HII regions. Also, maps of the line ratios show complex variations of the ionization conditions within HII regions. All this information is compiled in a new catalog for HII regions. The objective of this database is to provide a complete sample which will be used to study the whole parameter space covered by the physical conditions in active star-forming regions.

**Key words:** galaxies: individual: NGC 628, galaxies: spiral, galaxies: star formation, galaxies: HII regions, galaxies: diffused ionized gas, galaxies: nebular abundances, catalogues: HII regions, instrumentation: IFTS, IFTS : SITELLE

## 1 INTRODUCTION

The study of the ionized gas components in galaxies, for instance the population of HII regions as well as the diffuse ionized gas (DIG, also referred as the diffuse warm ionized medium; WIM), helps gathering important clues on the mechanisms that drives star formation and galaxy evolution. The gas emission lines are sensitive to the physical conditions in the interstellar medium (ISM) and their relative intensities probe underlying mechanisms involved in ionization processes. One predominant example related to the ISM ionization are the recent star formation sites where massive

stars act as the main source of ionizing photons. Gas ionization can also be triggered by other sources such as the energetic emission released by an active galactic nuclei (e.g. Ho 2008; Davies et al. 2014), the global evolved stars contribution to the heating of the ISM (e.g. Flores-Fajardo et al. 2011), different sources of small- and large-scale shocks in the ISM (e.g. Allen et al. 2008), etc.

The gas strong emission lines can be observed at cosmological distances, allowing the study of various star-forming environments through time. Establishing reliable HII region and DIG physical characteristics are therefore key elements in probing galaxy's chemo-dynamical evolution and improving star formation models. The extraction of these physical characteristics often involves photoionization codes, like MAPPINGS (Sutherland & Dopita 1993; Nicholls et al.

\* E-mail: r-nepton@cfht.hawaii.edu

2013) and CLOUDY (Ferland et al. 1998). These codes are used to model the complex interaction between the ionizing spectrum for different sources and the ISM. To constrain photoionization models, one needs spatially resolved star-forming region spectra including a set of different emission lines.

From an historical perspective, imagers and Fabry-Pérot instruments were often used to sample simultaneously a large number of HII regions in nearby galaxies. Imagers combined with different narrow-band filters allow us to target a few important emission lines and continuum windows (used to isolate the emission line flux from the presence of underlying stellar and nebular continuum; Mollá et al. 2009, Sánchez et al. 2011). Nevertheless, imaging techniques are limited by the number of emission lines accessible and are also affected by problems related to the spectral shift of the lines due to nebular and galactic dynamics, which prevent the accurate measurement of the lines. High-resolution spectra produced from Fabry-Pérot interferometers can provide additional information on stellar and gas dynamics. However, as their spectral range is limited, Fabry-Pérot interferometers were mostly used for the observation of one emission or absorption line. For this reason, most of the complex spectral analysis of extragalactic HII regions have been performed using slit spectrographs data, as they enable the accurate measurements of multiple emission lines over a wide spectral window. More recently, integral field spectrographs (IFS) offered a breakthrough by giving simultaneously spectral and spatial information on extragalactic HII regions. Still, the incomplete spatial coverage of these instruments is not convenient for a detailed study of extragalactic HII regions and to extract some of their intrinsic properties (e.g. total luminosity and morphology).

Some fundamental problems have been outlined from the analysis of extragalactic HII and DIG regions in nearby galaxies with integral field spectroscopy:

1) The lack of spatial resolution is preventing us from resolving individual HII regions and is imposing a great limitation on the scale of the physical processes studied. Even when analysing the large scale properties of galaxies, it has been shown that the gas abundance  $[O/H]$  gradient (derived from emission line diagnostics) is affected by a low spatial resolution, resulting in an artificial flattening of the gradients with respect to the redshift (Yuan et al. 2013; Mast et al. 2014). In addition, the lack of spatial resolution induces an attenuation on the extinction correction factor obtained from the Balmer decrement in integrated spectra as the extinction is biased toward the brightest and less dusty regions (Vale Asar et al. 2014). As a result, the derived star formation rate (SFR) and stellar mass content of HII regions are only upper limits.

2) A variable contribution from the superimposed DIG emission is often pointed out as a source of uncertainties when trying to extract the HII region properties (Blanc et al. 2009; Kreckel et al. 2016).

3) A degeneracy effect between the age of the HII regions and the under-sampling of the massive end of the initial mass function (IMF) precludes proper modeling of the ionized gas (Villaverde et al. 2010). Without resolving the stellar content, additional information on the ionization structure surrounding the stars is required using photoionization models to determine the precise stellar content of the regions.

4) Most of the diagnostic tools proposed to gather the abundances and other ionized gas properties are designed for integrated spectra (i.e. at low spatial resolution) and are calibrated using a small, sometimes biased, sample of HII regions with well defined properties. They are therefore limited tools, not representative of a large variety of environments within galaxies, and are not suited for a desired detailed analysis of resolved HII regions.

To overcome these numerous issues, we have conducted new observations of the nearby spiral galaxy NGC 628 with SITELLE, the Canada-France-Hawaii Imaging Fourier Transform Spectrograph (IFTS). SITELLE allows a high-spatial resolution (35 pc) over the whole galaxy disc (FOV:  $11' \times 11'$ ) with full coverage (100% filling factor). NGC 628 is a well known spiral galaxy seen almost face-on. It has been widely observed by others with various instruments. For instance, Rosales-Ortega et al. (2011) and Sánchez et al. (2011) performed a spectral analysis and studied the global properties (abundance gradients) of NGC 628 using a mosaic of the PPAK IFS ( $\sim 6'$  circular aperture) with individual fiber spectra and 94 selected apertures. Berg et al. (2015) used the Multi Object Double Spectrograph (MODS) to target 62 specific HII regions over the galaxy disc and investigated the abundance dispersion using direct temperature measurements from the auroral line. Grasha et al. (2015) used multiple Hubble Space Telescope broad band UV and optical images over two  $2.7' \times 2.7'$  fields in the disc of NGC 628 to identify 1392 young stellar cluster candidates ( $< 100$  Myr) and studied their size, mass and age, and the concentration of the stars embedded in the clusters. More recently, with the Multi-Unit Spectroscopic Explorer (MUSE), Kreckel et al. (2016) sampled 391 HII regions at the spatial resolution of 35 pc, analysed the DIG contribution, and studied the differences between the HII region properties in the arms and inter-arm regions. These previous studies have targeted different science goals and their contribution to the understanding of star-formation in galaxies is notable. Complementary to these studies, we believe that SITELLE has the potential to overcome several of the problems related to sample selection biases, the lack of spatial resolution, the contribution of the DIG, as well as to explore line ratio variations in the ISM with greater details.

The spectral datacubes obtained for this study with SITELLE triggered the development of new analysis tools tailored to its unique capabilities. In this paper, we present our approach for the systematic analysis of the emission line spectra of a large sample of HII regions observed with a high-spatial resolution. Our results are meticulously compiled in a general catalog for the HII regions which is made available to the entire astronomical community. Our immediate goal is to demonstrate the impact of the spatial resolution, mainly through the evaluation of the DIG background and the effect of sampling on characterizing the HII regions.

This paper is the first of a series where the systematic study of many nearby galaxies will be done with SITELLE to enlarge the domain of HII region physical parameters analysed. All the data gathered for the HII regions will be added to the catalog. It aims to be the largest and most detailed spectroscopic study of star-forming region properties in different galactic environments, and represents an important statistical tool to study small-scale processes in chemical enrichment and mixing; the balance between ionizing photons

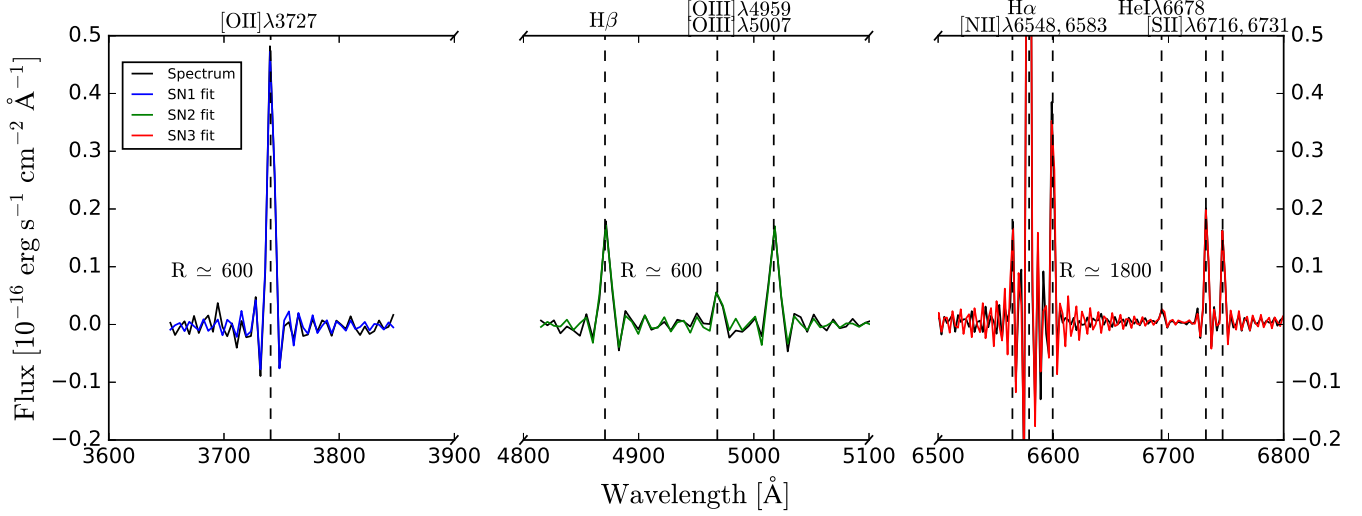


**Figure 1.** Continuum subtracted spectrum of an HII region in NGC 628 extracted from the datacubes using a circular aperture with a radius of  $1.6''$ , centered at RA 01h36m53.1s and DEC  $+15^{\circ}48'04.8''$ . The fits obtained with ORCS for the emission lines (§ 3) are shown. Note that SITELLE's line profiles are fitted using a sine cardinal function.

absorbed by the gas, the UV flux observed from a young population and the overall extinction; the DIG in relation with HII regions; the star formation efficiency and rate directly from the gas and stellar population characteristics; and the massive stars IMF in different environments. This catalog is tailored for the development of new diagnostics with photoionization codes and for the study of HII regions and their content at different spatial resolution.

Sections 2 and 3 describe the observations and the technique used to properly measure the gas emission lines. Section 4 focuses on the HII region definition, while Section 5 presents the luminosity function, morphology, and size of the regions. Section 6 presents the emission line ratios measured in individual spaxel within HII regions, as well as global ratios for each region for comparison with the literature. The results, along with the database content, are summarized in Section 7.

## 2 OBSERVATIONS AND DATA REDUCTION

NGC 628 was observed with SITELLE (Spectro-Imageur à Transformée de Fourier pour l'Étude en Long et en Large des raies d'Émission) at the Canada-France-Hawaii Telescope during the instrument commissioning and science verification runs in August 2015 and January 2016. Table 1 gives the main observing parameters. SITELLE is a Michelson interferometer inserted, with an inclination, into the collimated beam of an astronomical camera system (Drissen et al. 2014). Its main advantages, compared to other IFS, include a large field-of-view (FOV:  $11' \times 11'$ ) with complete spatial coverage, a high resolution power up to  $R \simeq 10\,000$ , and a broad wavelength range from 3500 to 9000 Å with an excellent efficiency all the way to the blue part of the spectrum. SITELLE is equipped with two E2V detectors ( $2048 \times 2064$  pixels, resulting in a mean pixel scale of  $0.321'' \times 0.321''$ ). Filters are necessary with SITELLE in order to reduce the noise in a selected bandpass. A raw datacube from SITELLE

**Table 1.** Observing Parameters

Filter	SN1	SN2	SN3
Spectral range [Å]	3640-3850	4840-5120	6480-6860
Observing date	2016/01/13	2016/01/11	2015/08/09
Exposure time/step [s]	73.0	103.3	25.0
Number of steps	105	138	323
Total exposure time [h]	2.13	3.96	2.24
Mean resolution R	$\sim 600$	$\sim 600$	$\sim 1800$
Image Quality [arcsec]	1.28	0.96	0.90

is composed of a sequence of images (one for each position of the movable mirror) that, when taken together, results in more than 4 million interferograms (one interferogram for each pixel of the detectors). After the data reduction, SITELLE produces 4 million spectra in a single datacube for a selected filter.

For this project, three filters have been used : SN1, SN2, and SN3; Table 1 gives the spectral range and resolution adopted for each filter. These configurations enabled the measurement of multiple strong emission lines: [OII]λ3727, Hβ (4861 Å), [OIII]λ4959, [OIII]λ5007, [NII]λ6548, Hα (6563 Å), [NII]λ6583, HeIλ6678, [SII]λ6716, and [SII]λ6731. Figure 1 shows the integrated spectrum in all three filters for one HII region. Figure 2 shows the deep image produced by adding, for each pixel, the whole signal from the three filters together with an enhanced contribution of the Hα intensity map extracted from the line fitting procedure (as described in § 3). SITELLE's FOV was slightly offset from the galactic center of NGC 628 in order to cover a vast portion of the disc as well as the extended northern spiral arm; the FOV was centered at RA 01h36m46.2s and DEC  $+15^{\circ}48'42.8''$ .

The data reduction was performed using the fully-parallelized reduction software ORBS (data-release 1) specifically developed for SITELLE (Martin 2015). The data reduction process requires additional calibrations from the instrument. Typical flat (using a white light source) were ac-



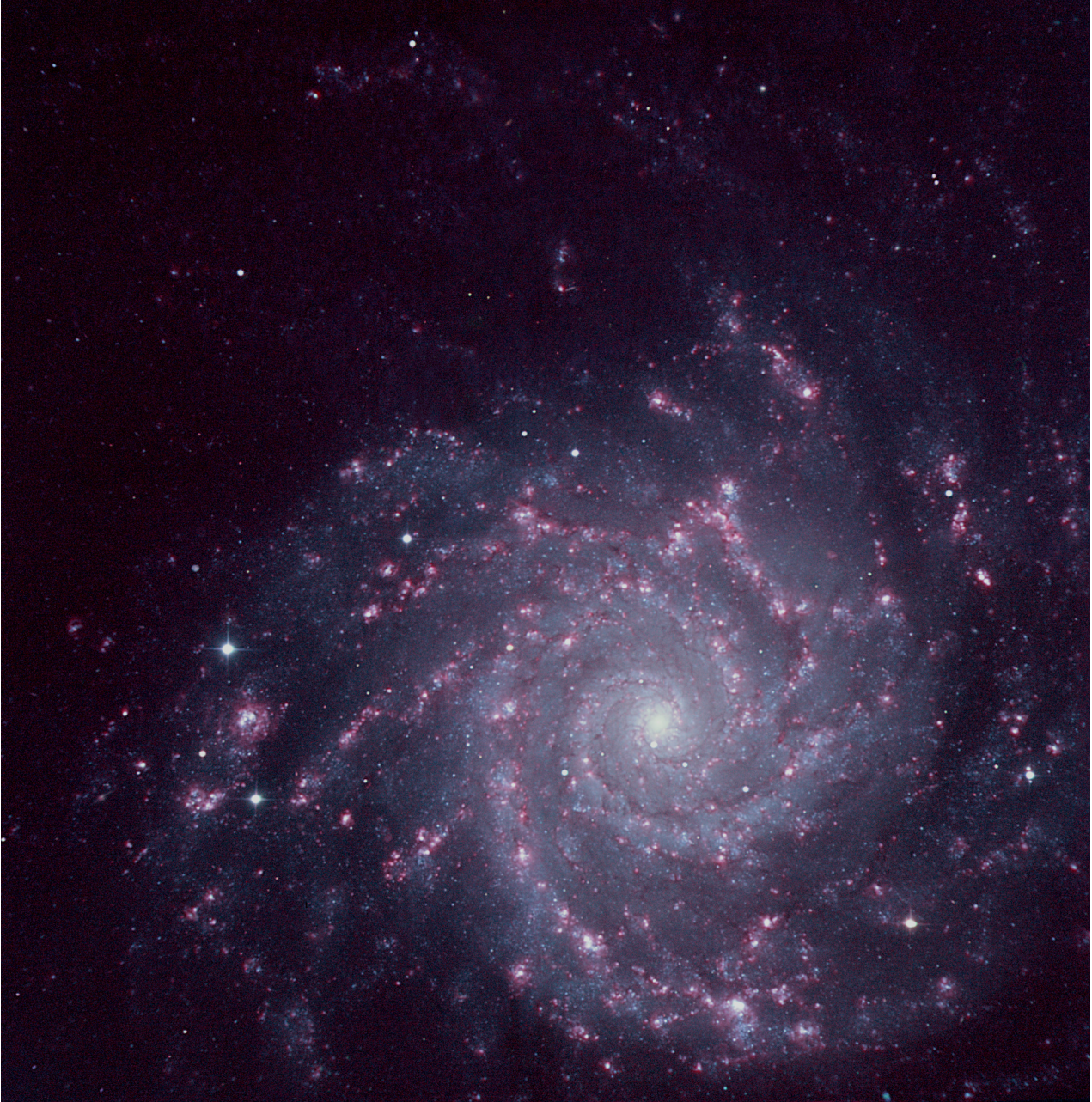


**Figure 2.** SITELLE’s deep image of NGC 628. For each pixel, the information from the three filters was summed together along with the  $H\alpha$  intensity map. Adding the  $H\alpha$  map highlights the ionized gas emission regions (in red on the image). North is up and East is left. The FOV is  $11' \times 11'$  centered on RA 01h36m46.2s and DEC  $+15^\circ 48' 42.8''$ .

quired during each nights and a pre-scan section of the CCD was preserved to measure the bias contribution in each exposure. The flux calibration was performed using a datacube of the standard star GD 71 secured with each filter to define the global transmission function. The spectral calibration was done using an Helium-Neon laser datacube acquired during daytime. For the SN3 filter (at higher R), greater precision on the spectral calibration was obtained using the centroid position of sky lines (§ 3.1). Additionally, three flat datacubes were acquired using a white light source (one for each filter) in order to apply high-order phase correction in the data reduction process (Martin et al. in prep.). To match

the image quality obtained for the different datacubes (see Tab. 1) and attenuate the impact of a small misalignment of the datacubes, we applied a Gaussian convolution (with a  $\text{FWHM} = 3$  pixels) on all the images within the datacubes. We did not correct for the Milky Way extinction knowing that it is very small ( $E(B-V) = 0.062$  according to NED<sup>1</sup>).

<sup>1</sup> The NASA/IPAC Extragalactic Database (NED) is operated by the Jet Propulsion Laboratory, California Institute of Technology, under contract with the National Aeronautics and Space Administration.





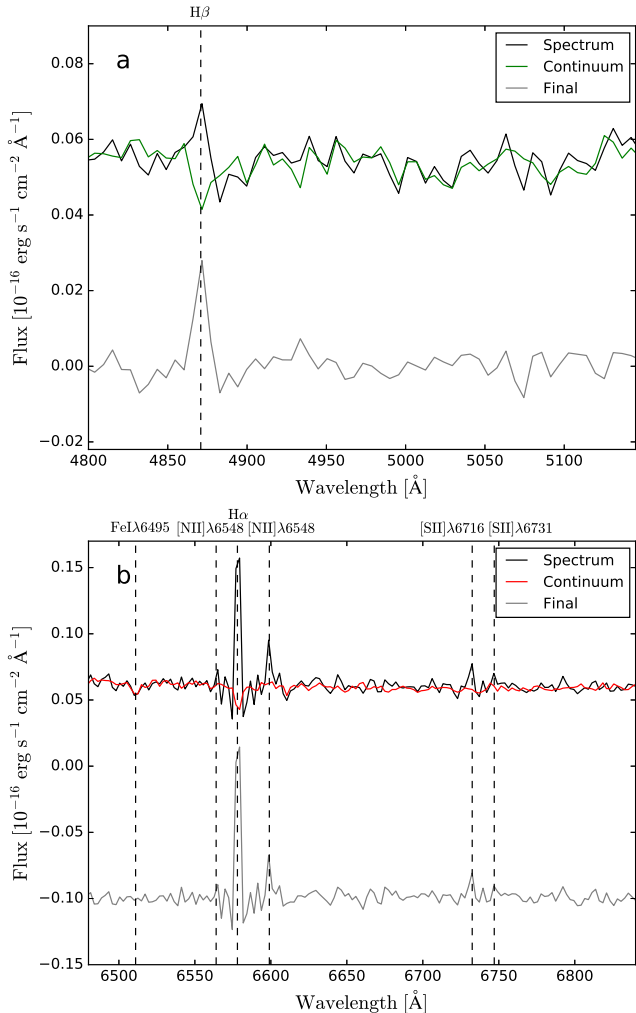


**Figure 4.** The spectrum for one pixel in a faint HII region close to the galaxy center extracted at RA 01h36m41.5s and DEC +15°46′57.0″ from the SN2 (a) and SN3 (b) datacubes. The reference spectrum used to represent the galaxy stellar populations along the line of sight of the HII region is shown shifted to the pixel velocity and scaled to the level of the continuum. The residual after subtraction is shown at the bottom.

dispersion along the disc. Nevertheless, NGC 628 is not a massive galaxy and we are therefore confident that, at the resolution of 35 pc, the use of the reference spectrum does not introduce an important artifact due to a stellar population variation with the galactocentric radius compared to the improvement gained for the emission line measurements. This is well supported by Rousseau-Nepton (2017), where longslit spectroscopy (between 3500 and 7500 Å) across the galaxy disc and nucleus has shown only a very small variation of the absorption lines from normalized spectra at different radii.

Figures 4 and 5 show the effect of the stellar population reference spectrum subtraction for the Hβ (SN2) and Hα (SN3) emission line of one spaxel selected in the center of a faint HII regions, and for the Hα (SN3) emission line in a DIG region. The reference spectrum for the disc stellar populations is superimposed to the spectrum of these regions in the figures. The residual spectrum obtained after

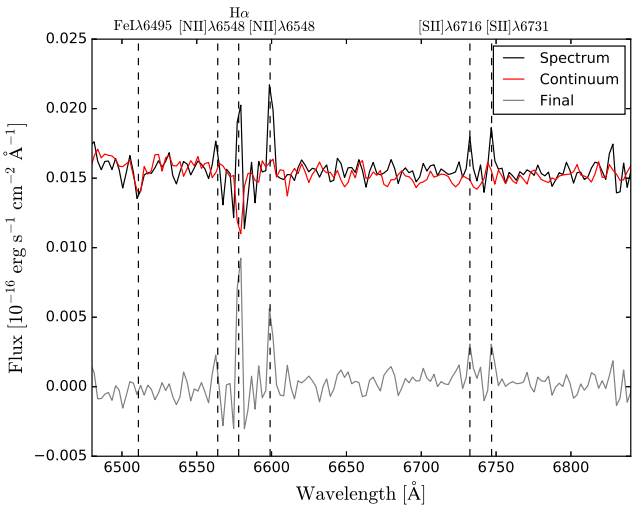


**Figure 5.** The spectrum of the DIG extracted from the SN3 datacube using a circular aperture with a radius of 8.0″, centered at RA 01h36m43.3s, DEC +15°46′57.9″. The reference spectrum used to represent the galaxy stellar populations along the line of sight of the HII region is shown shifted to the pixel velocity and scaled to the level of the continuum. The residual after subtraction is shown at the bottom.

the subtraction is also shown. It clearly demonstrates that the subtraction of the stellar population reference spectrum is important in order to measure accurately the emission lines in all spaxels.

### 3.5 Line Fitting Procedure

For each spaxel in all three datacubes, the emission lines are fitted simultaneously using the extraction software ORCS (Martin et al. 2015<sup>3</sup>). This software was specifically created for SITELE and therefore uses sinc-shaped line profiles. ORCS’ output map for each line includes the maximum intensity, FWHM, velocity, continuum level, all the corresponding uncertainties, the SNR, as well as the  $\chi^2$  of the fit. These parameters can then be used to get the flux and its uncertainty maps for all lines. Examples of the line fits are shown in Figure 6 for all three filters. The fluctuation seen in the residual underneath Hα is caused by the subtraction of the galaxy stellar contribution which, as we discussed in the previous section, may not be perfectly well adapted (in content and velocity dispersion). But, as seen here, the impact on the line fitting is negligible (< 1%). Appendix A contains the resulting flux maps for all the lines. It also shows the velocity map obtained by fitting simultaneously all the SN3 emission lines with ORCS.

## 4 REGION DEFINITION

Although one can study individual spaxel within an ionized gas region in a nearby galaxy like NGC 628 with SITELE, some properties must be investigated using their integrated

<sup>3</sup> <https://sourceforge.net/projects/orb-orcs/>

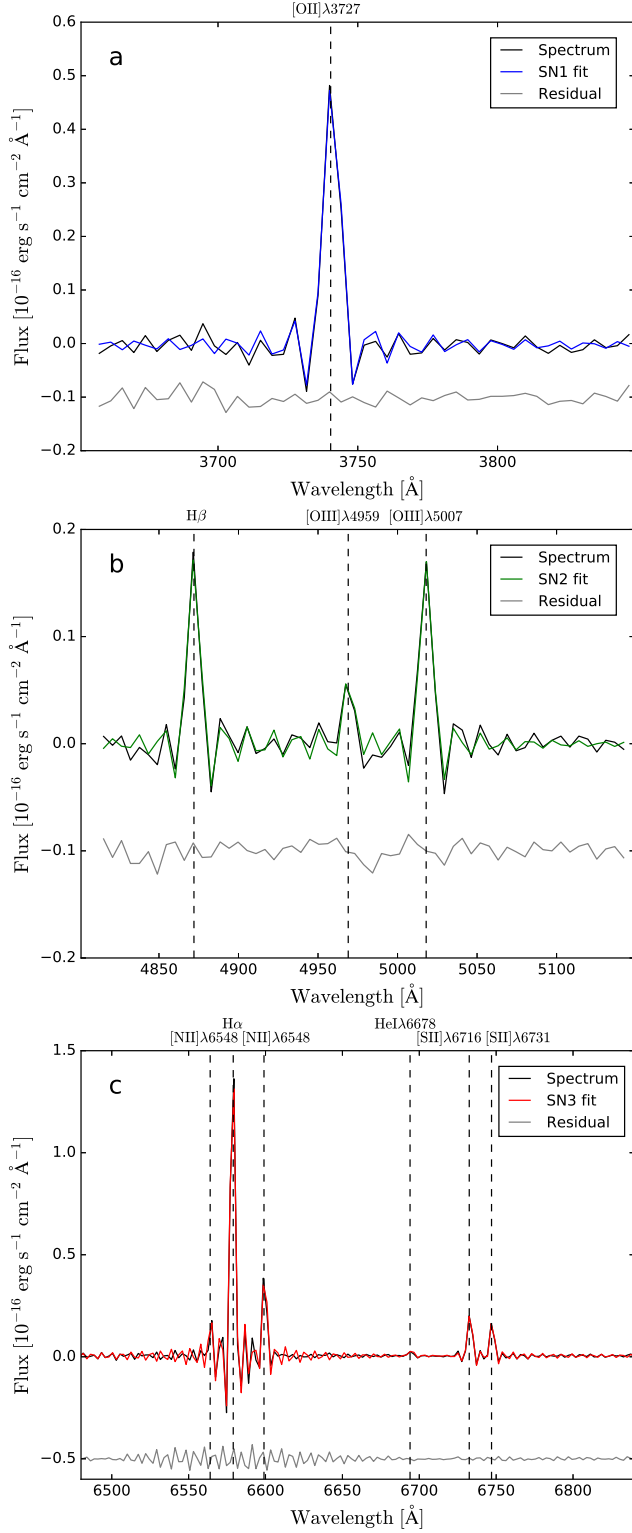


**Figure 6.** The spectrum of an HII region combining the spaxels within a circular aperture with a radius of  $1.6''$  centered at RA 01h36m53.1s and DEC  $+15^{\circ}48'04.8''$ . The SN1 filter in a, SN2 in b, and SN3 in c. The fit obtained with ORCS and the residual after the fit subtraction are shown.

flux (e.g. the region luminosity function) and a clear description of their morphology (e.g. their size). It is therefore necessary to distinguish which pixels belong to a given HII region. A new code is presented here for identifying the position of the ionizing source associated to a region and its boundaries. Compared to other existing codes, like those based on the H $\alpha$ -continuum-subtracted images and a standard-fixed-threshold-photometry method, such as the percent-of-peak-photometry method (McCall et al. 1996), or HIIphot (Thilker et al. 2000, 2002), this new code gives us flexibility in defining regions and their DIG background.

Our method proceeds with multiple steps : 1) the identification of the emission peaks, 2) the determination of the zone of influence around each emission peak, and 3) the definition of the outer limit of an HII region and its DIG background. These operations are done prior to the extinction correction, to avoid introducing unnecessary noise. The different steps of our method are described below.

**Definition of the Peaks** - The first step involves adopting a definition for the emission peaks and identifying all of positions. We use a combination of the H $\alpha$ , H $\beta$ , and [OIII]λ4959,5007 continuum subtracted images. This choice is motivated by the increased SNR of the combined images. Moreover, as found from our high-spatial, the maximal intensity of these three lines coincides with the center of the HII regions. An emission peak is identified for a pixel when: 1) the pixel intensity is greater than the intensity of at least 5 immediate surrounding pixels (i.e. all these pixels must be in contact with the maximum intensity pixel), and 2) the total intensity in a  $3 \times 3$  pixels box centered on the emission peak is above the adopted detection threshold. This threshold is fixed by the  $3\sigma$  noise level of the H $\alpha$ +H $\beta$ + [OIII] flux map (a slightly different value is adopted for each of the CCD quadrant according to their individual noise level). Furthermore, if two emission peaks are separated by a distance smaller than the image quality of the observation, only the brightest peak is preserved. For each so-defined emission peak, two values of its mean flux are evaluated considering a circular aperture with a radius of 1 and 2 pixels centered on the emission peak. The peak is rejected when the mean flux does not significantly decrease between the small and large aperture (i.e when a drop less than  $\sim 2\%$  per pixel is seen for the bright regions, with a flux  $F_{H\alpha} \simeq 1 \times 10^{-15}$  erg s $^{-1}$  cm $^{-2}$ , and when a drop less than  $\sim 5\%$  is seen for faint regions). This criterion allows us to remove false identifications inside a bright ionized gas region, that are likely to be associated with small surface brightness variations, while eliminating false detections due to random noise fluctuations. To find the accurate position of their centroid, a 2D Gaussian model is fitted on the remaining emission peaks using the IDL procedure MPFIT2DPEAK. A total of 4285 emission peaks is finally detected for NGC 628 with our extraction technique. After a visual verification of a representative group of emission peaks, we estimate that only a small fraction,  $\sim 0.5\%$ , of these detections are false detections (not an ionized gas region). It is also important to note that most of the remaining regions are HII regions while a few percentage may be supernova remnants and planetary nebulae, as it will be demonstrated by their location within the BPT



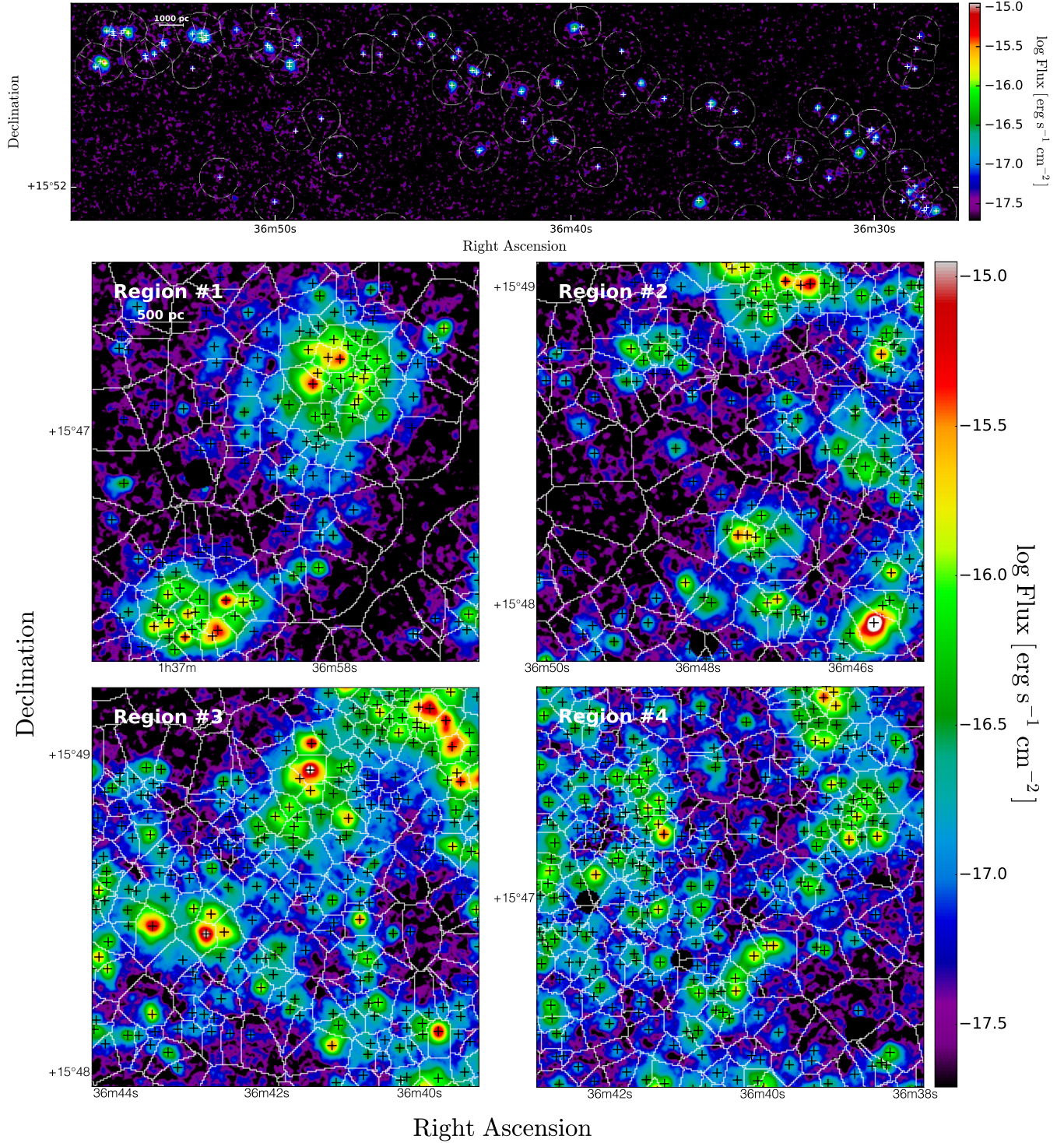


**Figure 7.** Examples of ionizing sources and their zone of influence in the galaxy northern arm (up) and in four reference regions of the galaxy (bottom) drawn over the  $\text{H}\alpha + \text{H}\beta + [\text{OIII}]\lambda\lambda 4959, 5007$  continuum subtracted image. The location of the four reference regions may be seen on the  $\text{H}\alpha$  image in Figure A3. The centroid position of each emission peak detected is identified with a cross. The white contours define the zones of influence surrounding the emission peaks.

diagrams in Section 7.

**Zone of Influence** - Figure 7 shows the emission peaks and their zone of influence for a section of the northern arm and for four reference regions selected in the galaxy disc.

We name the area that is influenced by the ionizing photons from an emission peak, the zone of influence. It is defined by studying the distance between each pixel and all its surrounding emission peaks. In order to consider all extend possible for the regions, we looked over a maximum distance

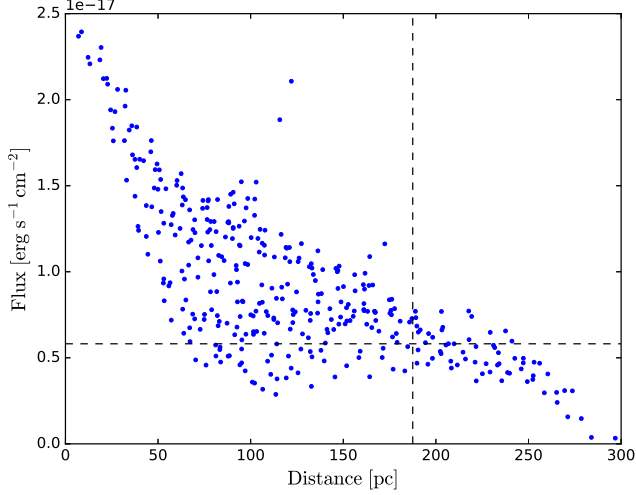


**Figure 8.** The  $H\alpha$  flux for the individual pixels of the HII region ID 2688. Each pixel included within the zone of influence is represented by a dot. The vertical line indicates the outer limit of the region found from the total flux profile (Fig. 9) and the horizontal line gives the intensity level of the DIG background.

of 425 pc around each pixels (corresponding to 30 pixels). This distance is greater than the maximal outer limit distance found for the regions of NGC 628, as seen in the next paragraph. Most of the time a pixel is then associated to the closest emission peak. In the case of multiple emission peaks at the same distance (considering a distance uncertainty given by the image quality), the pixel is then associated to the emission peak with the maximum intensity. The more distant pixels associated to an emission peak define the boundary of the zone of influence for this ionizing source.

#### **Outer Limit of a region and the DIG Background**

- Within the zone of influence of an ionizing source, the intensity profile changes rapidly. Figure 8 shows, for a faint region, the  $H\alpha$  flux of all the individual pixels included inside the zone of influence as a function of their distance to the emission peak centroid. Figure 9 presents the total flux profile for this region. The total flux is calculated by summing the flux of the pixels within a circular annulus 25 pc thick centered on the emission peak. The outer limit of the region is then defined at a distance where the slope of the total flux profile decreases by less than 2% within the zone of influence. The DIG background is given by the median intensity value for all the pixels included in an annulus 50 pc thick centered at the position of the outer limit. The 2% threshold was selected after a few iterations: a larger value overestimates the DIG background for numerous HII regions, whereas a smaller value is not sensitive to variations of the slope. As a result, a limit is often never reached. In Figure 9, the effect of the DIG background subtraction on the total intensity profile is also shown for the same faint region selected here as an example.

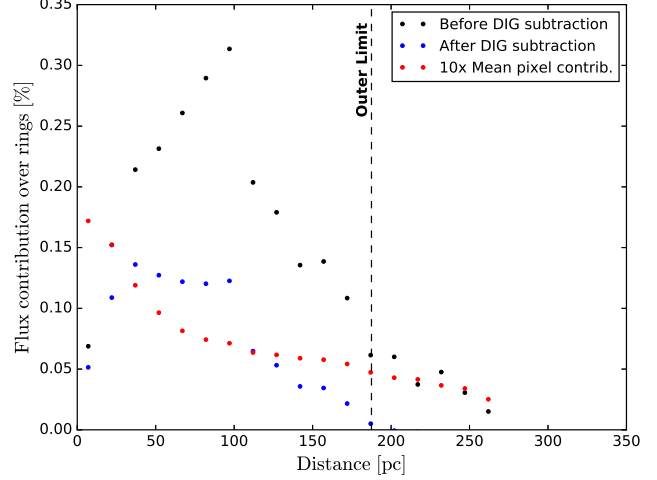


**Figure 9.** The  $H\alpha$  total flux profile of the HII region ID 2688. The total flux observed (black dots) is calculated within annuli centered on the ionizing source within the zone of influence. The vertical line indicates the outer limit, where the slope of the total flux profile decreases by less than 2%. Blue dots show the total flux profile after the subtraction of the DIG background. The mean pixel contribution to the flux profile is shown in red (enhanced by a factor of 10).

## **5 LUMINOSITY FUNCTION, MORPHOLOGY AND SIZE OF THE HII REGIONS**

### **5.1 Extinction Correction**

To evaluate the color excess  $E(B - V)$ , we used the following equation:

$$E(B - V) = \frac{2.5}{1.07} \log \left( \frac{F_{H\alpha}/F_{H\beta \text{ obs}}}{2.87} \right), \quad (1)$$

with  $A_\lambda = 2.5 \log I_\lambda / I_{\lambda 0}$ , and  $E(\beta - \alpha) / E(B - V) = 1.07$  (extracted from the extinction curve of Cardelli et al. 1989), and where  $F_{H\alpha} / F_{H\beta \text{ obs}}$  is the observed flux ratio of the two main Balmer lines. We adopted a theoretical  $F_{H\alpha} / F_{H\beta}$  ratio of 2.87 (as expected for the Case B of Osterbrock 1989, at a temperature of 10 000 K).

Using the previous equation and the relation  $A_V = 3.1 E(B - V)$ , we obtained the pixel-by-pixel extinction for NGC 628 from SITELE's  $H\alpha$  and  $H\beta$  maps. The extinction map is shown in Figure 10, where only the spaxels with a  $3\sigma$  detection for both lines have been considered. Figure 11 presents the extinction as a function of the galactocentric radius for all the spaxels (the observed radii was deprojected using a galaxy inclination of  $21^\circ$  from NED). The extinction is clearly decreasing as we look further out in the disc. Fitting a polynomial function through this plot, we obtained the following relation:

$$A_V = 0.0008386 R_G^3 - 0.02267 R_G^2 + 0.08398 R_G + 0.8541. \quad (2)$$

The data highest density distribution (Fig. 11 in green) shows values in good agreement with Berg et al. (2015) of  $A_V \simeq 0$  to 1.28 mag, for their sample of 45 HII regions. The mean value obtained for our sample is:  $A_V = 0.86 \pm 0.81$  mag, lower than the mean value of  $1.24 \pm 0.76$  mag found by Sánchez et al. (2011) with IFS data in the inner part ( $R_G \leq 9$  kpc) of the galaxy.



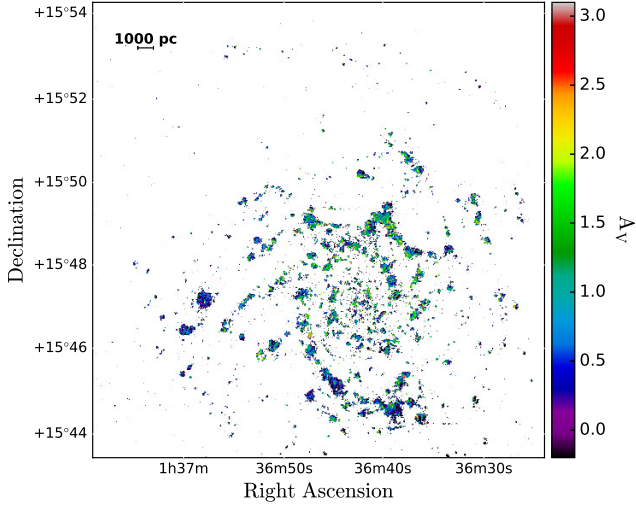


**Figure 10.** The extinction map obtained from SITELE’s  $H\alpha$  and  $H\beta$  line ratio for each spaxel. Only spaxels with a  $3\sigma$  detection limit for both lines are shown. The three giant HII regions, out in the disc to the South and East, display on average a smaller extinction value.

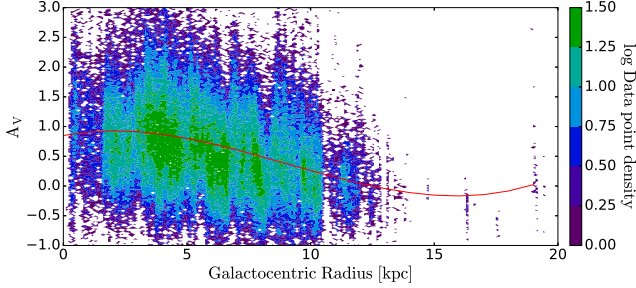


**Figure 11.** NGC 628 extinction gradient. The extinction for all the spaxels (with  $\text{SNR}_{H\alpha}$  and  $\text{SNR}_{H\beta} > 3$ ) is plotted as a function of their galactocentric radius. The plot is color coded according to the spaxel density.

A close examination of the extinction map as displayed in Figure 10 suggests significant fluctuations in the extinction within individual HII regions. Furthermore,  $\sim 10\%$  of the spaxels have an observed ratio  $F_{H\alpha}/F_{H\beta}$  below the theoretical value (this is seen in Fig. 11 for  $A_V < 0$ ). Some tests were done to investigate the cause of these variations and the low flux ratios. By combining many spaxels within a region, we used various aperture sizes to see the impact of atmospheric refraction on the measured flux ratio. The accuracy of the flux calibration and the alignment of the datacubes was also tested. Although these effects can increase the flux uncertainty, we find that they can not be hold responsible for all the spaxels with a Balmer line flux ratio below the theoretical value. A simple explanation often proposed for low Balmer line flux ratios invokes the low SNR of the  $H\beta$  line. But this is not sufficient here as we estimate that only  $\sim 4\%$  of the spaxels with a ratio  $F_{H\alpha}/F_{H\beta}$  below the theoretical value have  $\text{SNR}_{H\beta} < 10$  (including the effect associated to atmospheric refraction, flux calibration, and alignment of the datacubes). Therefore, some of the low Balmer line flux ratios, along with the extinction variation

seen inside an HII region itself, could be real and possibly related to the change of the physical parameters (e.g. the electron temperature and density) within that region. The theoretical Balmer line flux ratio can reach 2.75 at 20000 K according to Osterbrock (1989). Depending on the morphology of the HII regions, the dust backscattering (O’Dell et al. 2017) can also contribute to the observed variation of the flux ratio. SITELE’s data is therefore revealing the detailed physical conditions within HII regions and their close surrounding.

Using the extinction law of Cardelli et al. (1989), we corrected all our flux maps. The relation given by Equation 2 was used for the spaxels where no precise extinction was measured (for  $A_V < 0$  and with  $\text{SNR}_{H\alpha}$  or  $\text{SNR}_{H\beta} < 3$ ). As the extinction correction is subject to uncertainties, line ratios (as presented in § 6) built using lines that are far away from each other (i.e. lines from different filters) have also greater uncertainties.

## 5.2 HII Region Luminosity Function

The total  $H\alpha$  flux of an HII region is obtained by summing the flux of all the pixels up to the outer limit radius, and after subtraction of the DIG background. Using a distance of 9.006 Mpc for the galaxy (NED), the total flux is then converted into the  $H\alpha$  luminosity. For some fainter regions, the central peak can be well detected but noise in the region’s boundary can produce a total luminosity below the initial detection threshold. Therefore, from the 4285 regions detected, 4158 have a  $\log(L_{H\alpha}$  in  $\text{erg s}^{-1}$ ) above the detection limit of 35.65.

The luminosity function from the complete sample of HII regions is shown in Figure 12. It follows the relation  $N(L)dL = AL^{-\alpha}dL$ , where  $N(L)dL$  is the number of HII regions with a luminosity in the range  $L$  to  $L+dL$ . The analysis was done by considering regions before and after the extinction correction. Bins of 0.05 in  $\log(L_{H\alpha}$  in  $\text{erg s}^{-1}$ ) were selected due to the data quality, allowing us to show a smooth and well-sampled curve. The luminosity function slopes derived with the extinction corrected data,  $\alpha_{cor} = -1.12 \pm 0.03$ , and without the correction,  $\alpha_{obs} = -1.10 \pm 0.04$ , are identical. The median luminosity is  $36.77 \pm 0.02$  for the observed data and  $36.95 \pm 0.02$  for the extinction corrected data. No break in the slopes is seen, as previously noticed at high luminosity, e.g. Bradley et al. (2006).

We looked for variations of the luminosity function with the galactocentric distance of the HII regions, separating them into two samples, one inside and one outside a radius  $R_{gal}$  of 6.5 kpc (in the case of the extinction corrected data only). This distance was first selected because it simply gives a nearly equal number of HII regions in both samples (2075 regions inside and 2083 regions outside 6.5 kpc). These two samples are also covering a different gas metallicity range, as already known from the metallicity gradient reported by several authors (e.g. Sánchez et al. 2011; Pilyugin et al. 2014; Berg et al. 2015) and as supported by the line ratios studied in Section 6. Figure 13 shows the resulting luminosity functions. We do not see a significant change in the slope of the function with respect to the radial position in the disc ( $\alpha_{> 6.5 \text{ kpc}} = -1.11 \pm 0.04$  and  $\alpha_{< 6.5 \text{ kpc}} = -1.14 \pm 0.05$ ). Regions in the central portion of



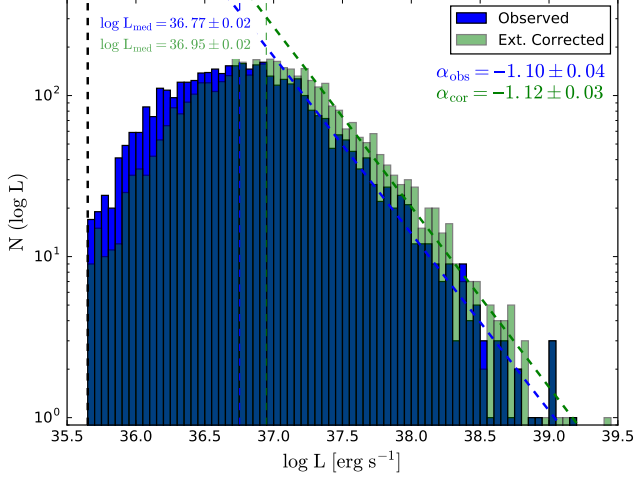


**Figure 12.** The luminosity function of the 4158 HII regions before (in blue) and after (in green) the extinction correction. The slope  $\alpha$  is evaluated in the luminosity range  $\log(L_{med})+0.2$  to 39.3 in both cases. The vertical lines in blue and green indicate the median value for each case. The vertical line in black shows the detection limit.

the disc ( $< 6.5$  kpc) are in general slightly brighter with a median value of  $\log L_{med} = 37.01 \pm 0.02$  compared to  $\log L_{med} = 36.86 \pm 0.02$  in the external portion of the disc. Brighter regions and less faint regions are seen in the central portion of the disc compared to the external disc. This could be the result of a crowding effect in the central disc, where many small regions overlap and are measured as one bright region. To evaluate if the level of crowding is different in both subsamples, the distance between two peaks was evaluated for the closest, the second closest, and the third closest peak for all the 4285 peaks in the sample. We found a median value for the distance between peaks of 110.0 pc at  $R_{gal} < 6.5$  kpc and 115.5 pc at  $R_{gal} > 6.5$  kpc for the closest, 159.5 pc at  $R_{gal} < 6.5$  kpc and 168.3 pc at  $R_{gal} > 6.5$  kpc for the second closest, and 198.6 pc at  $R_{gal} < 6.5$  kpc and 211.0 pc at  $R_{gal} > 6.5$  kpc for the third closest peak. The error for all median values is  $< 1$  pc if evaluated by moving the galactocentric radius threshold by 500 pc. Although small, this difference supports the idea that a crowding effect could explain the small differences observed in the luminosity functions presented in Figure 13.

Figure 14 shows the luminosity function for two samples of HII regions separated according to their DIG background. A threshold for the DIG surface brightness of  $2.05 \times 10^{-18} \text{ erg s}^{-1} \text{ cm}^{-2}$  over one pixel was used to separate the two samples. Although some very bright HII regions with a significant DIG background are not in the arms, the higher DIG background groups contains HII regions mostly located in the core of the spiral arms (as previously found by Kreckel et al. 2016). As the bright regions have brighter DIG background, it suggests that the main ionization source for the DIG is within the regions themselves, i.e. massive stars. When excluding spiral arm regions, we find that the DIG background level is correlated with the galactocentric radius, as higher DIG emission is measured in the regions closer to the galaxy center (see Fig. 15). This suggests that the evolved star background, more important in the galaxy

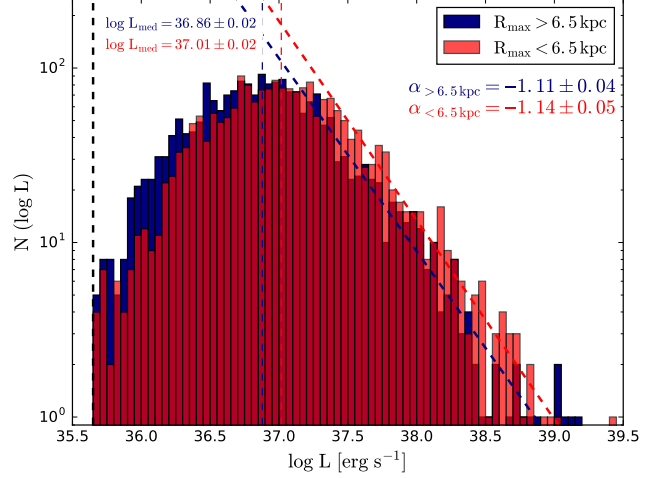


**Figure 13.** The luminosity function of the HII regions (extinction corrected) inside and outside a galactocentric radius  $R_{gal} = 6.5$  kpc. The slope  $\alpha$  is evaluated in the luminosity range  $\log(L_{med})+0.2$  to 39.1 for both samples (inside the 6.5 kpc radius in red and outside in blue). The vertical lines in red and blue indicate the median value of each sample. The vertical line in black shows the detection limit.

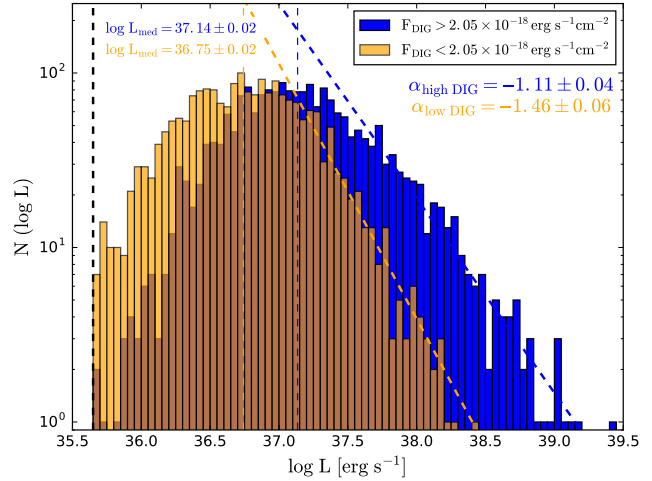


**Figure 14.** The luminosity function of HII regions (extinction corrected) as a function of their DIG background. The threshold for the DIG emission is  $2.05 \times 10^{-18} \text{ erg s}^{-1} \text{ cm}^{-2}$  over one pixel. The slope  $\alpha$  is evaluated in the luminosity range  $\log(L_{med})+0.2$  to 38.4 for the low DIG background sample (in orange) and in the range  $\log(L_{med})+0.2$  to 39.3 for the high DIG background sample (in blue). The vertical lines in gold and blue indicate the median value of each sample. The vertical line in black shows the detection limit.

inner region, is also a source of ionization for the inter-arm regions. The selected DIG threshold also ensures two samples with a similar size (2075 regions above and 2083 below the threshold). In this case, a significant difference is measured for both the median value and the slope of the luminosity functions (Fig. 14). The sample with a lower DIG background has lower values:  $\log(L_{med}) = 36.75 \pm 0.02$ , compared to  $37.14 \pm 0.02$  for the high DIG background regions, and a slope  $\alpha_{low DIG} = -1.46 \pm 0.06$ , compared to

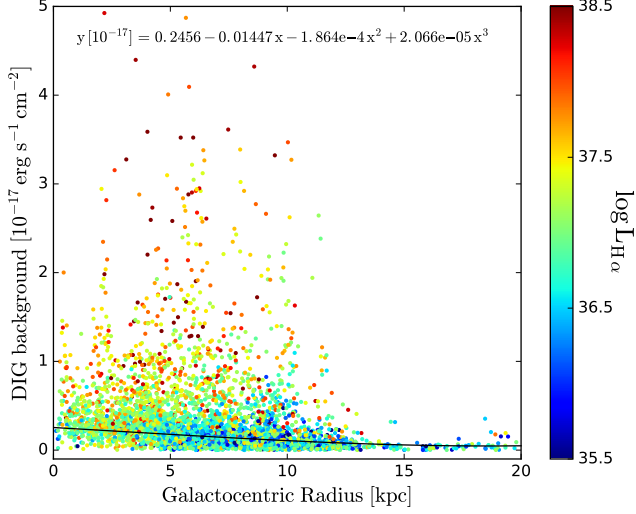


**Figure 15.** The DIG background from the  $H\alpha$  emission flux for each of the 4285 spaxels as a function of their galactocentric radius  $R_{gal}$ . The color scale is a function of the total  $H\alpha$  luminosity of the region where the spaxel is located as define in Section 5.2. The black line shows a polynomial fit to the data while excluding regions above  $5 \times 10^{-18} \text{ erg s}^{-1} \text{ cm}^{-2}$  (the relation from the fit is given on the plot).

$\alpha_{high DIG} = -1.11 \pm 0.04$ . The slope of the lower DIG background regions is similar to the slope found in M31 ( $\alpha_{M31} = -1.52 \pm 0.07$ ) by Azimlu et al. (2011). Therefore there is a clear relation with the DIG background and the average luminosity of the HII regions, here associating the DIG origin with the importance of the massive star population. But in the case of the lower DIG background regions, the change in the slope of the luminosity function and the correlation with the galactocentric radius suggest multiple origins for the DIG background.

### 5.3 Morphology of the HII regions

Constraining the morphology and the size of the HII regions requires modeling their intensity profiles in more details. The morphological classification of HII regions is often performed by eye, but with a large sample as obtained here, an automated approach was considered. At the spatial resolution of our survey ( $\sim 0.8''$  or 35 pc), we were mostly interested in obtaining the general shape of the regions and in separating compact from extended regions.

To establish the general shape of the HII regions, we divided them into four categories: symmetrical, asymmetrical, transient, and diffuse. Figure 16 presents an example for each category. Before explaining our criteria for the classification, we can see that the symmetrical region looks almost spherical on the  $H\alpha$  image and presents very low dispersion in its luminosity profile, as shown in Figure 17. The ionizing source (i.e. stellar populations) of this region is likely to be concentrated in the center with the surrounding gas equally distributed. The asymmetrical region shows an important emission peak but also a large variety of shapes diverging from the spherical case. In this case, the stellar content is expected to be either more dispersed or to encompass multiple clusters and/or the surrounding gas is not equally dis-

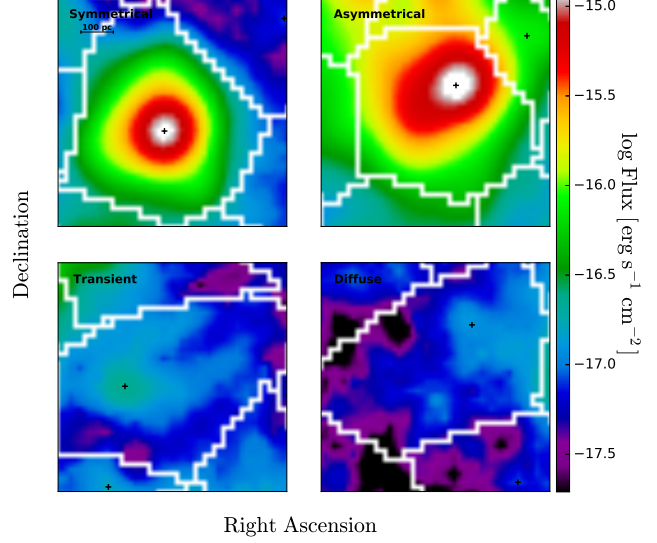


**Figure 16.** Examples of HII regions with different morphological classification. The four categories of HII regions are represented using the  $H\alpha$  image; the categories are identified in the left corner of each image. The ID of the regions selected, from top-left to bottom-right, are : 2437, 2987, 2688, and 834.

tributed in all directions. The diffuse region is less peaked and its intensity profile presents even more dispersion. The transient regions lie between the asymmetrical and the diffuse ones; the dispersion impedes our ability to distinguish between an asymmetrical region and a region with diffuse structures such as large filaments of ionized gas.

The HII region morphologies are fully quantified using the intensity profile. We selected a pseudo-Voigt function to fit the profiles (a linear combination of a Gaussian and a Lorentzian profile) using the Nelder-Mead method (Nelder & Mead 1965). The pseudo-Voigt profile is defined by the equation:

$$f(x, A, x_0, \sigma, \alpha) = \frac{1 - \alpha}{\sqrt{2\pi}\sigma_g} A e^{\frac{-(x-x_0)^2}{2\sigma_g^2}} + \frac{\alpha A}{\pi} \frac{\sigma}{(x-x_0)^2 + \sigma^2}, \quad (3)$$

where the constant  $A$  is the amplitude,  $\sigma_g = \sigma/\sqrt{2\ln 2}$ , and  $2\sigma = \text{FWHM}$ . The constant  $\alpha$  is a fraction revealing the relative importance of the Gaussian and the Lorentzian term to the profile. The centroid position ( $x_0$ ) was fixed to 0 as it is already constrained by our peak identification procedure. The use of a pseudo-Voigt function enables us to reproduce the observed  $H\alpha$  flux profile very well in the case of a peaked emission with a spherical morphology (the pseudo-Voigt profile is shown in Fig. 17 for the example selected). The fraction  $\alpha$  varies significantly from one HII region to another, and allowing us to recover the outer part of the profile more accurately than by using a simple Gaussian profile. A correlation coefficient ( $R^2$ ) for the fit was also evaluated for each HII region by considering the whole profile from the center to the outer boundary. Only 13% of the regions have a correlation coefficient  $R^2 < 0.5$  and 7% have a correlation coefficient  $R^2 < 0.3$ .

For each HII region, we used the pseudo-Voigt  $H\alpha$  intensity profile to evaluate the average pixel dispersion as a

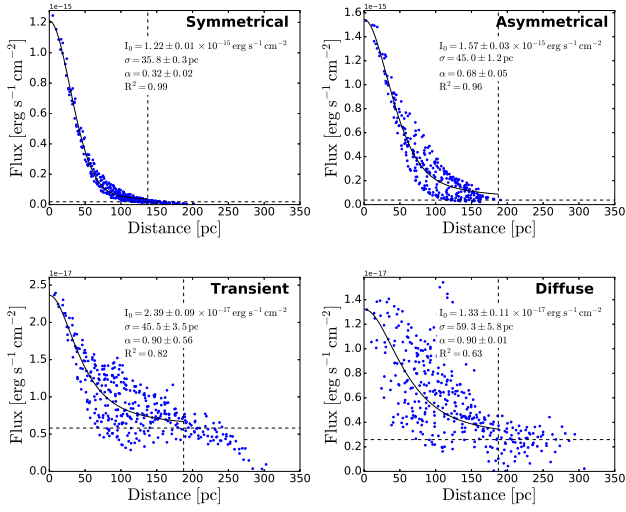


**Figure 17.** The  $H\alpha$  flux profile for the HII regions presented in Figure 16. The intensity for all the pixels included in the zone of influence are plotted as a function of their distance to the emission peak. The vertical line represents the outer limit and the horizontal line represents the DIG background. The black curve is the best  $\chi^2$  fit obtained using a pseudo-Voigt profile. The categories are identified in the right corner of each plot along with the fit parameters of the Equation 3 and the correlation coefficient  $R^2$ . The ID of the regions selected, from top-left to bottom-right, are : 2437, 2987, 2688, and 834.

**Table 2.** Dispersion thresholds for the morphological classification. The dispersion thresholds are given in % of the region peak value.

Category	Center <sup>a</sup>	Sigma <sup>a</sup>	Outer Limit <sup>a</sup>	Regions
Symmetrical	$\leq 6\%$	$\leq 6\%$	none	448
Asymmetrical	$\leq 6\%$	$> 6\%$	$\leq 3\%$	772
Transient	$\leq 6\%$	$> 6\%$	$> 3\%$	1785
Diffuse	$\geq 6\%$	$> 6\%$	none	1280

function of the distance over three 15 pc annuli: in the very center, at the position of  $1\sigma$ , and at the outer limit. We also evaluated the average pixel dispersion within these same annuli by using the mean value instead of the fitted profile. This second method was required for specific HII regions where the pseudo-Voigt profile could not properly fit the peak or the background intensity. The smallest dispersion values, evaluated using either the mean or the pseudo-Voigt fitted profile, were considered to assign a morphological category to an HII region. The dispersion thresholds for all four categories were first selected arbitrarily (by eye) to finally follow the rules listed in Table 2.

Figure 18 shows, for each morphological category individually, the integrated  $H\alpha$  luminosity of the HII regions as a function of the  $\sigma$  value of their pseudo-Voigt fitted profile. The symmetrical morphology category contains on average HII regions that are bright and more compact, while the diffuse category contains HII regions that may be among the faintest ones and among the most extended. Asymmetric regions, which may contain multiple sources, are among the brightest ones.

Figure 19 shows the integrated  $H\alpha$  luminosity of the

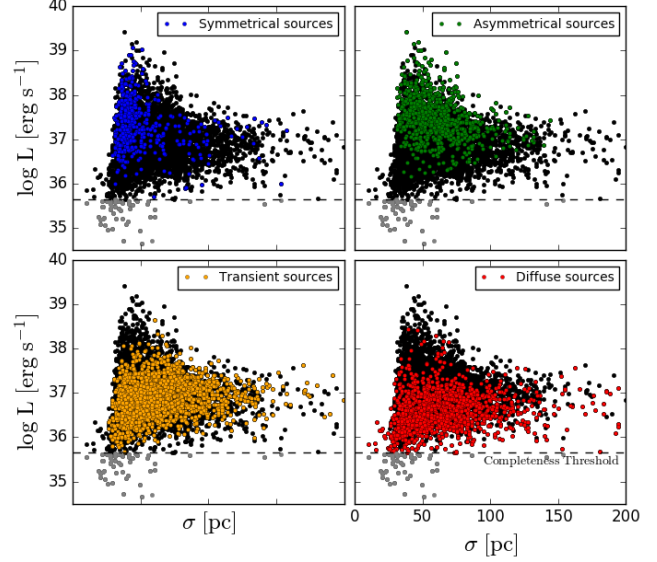


**Figure 18.** The HII region  $H\alpha$  luminosity distribution for the four morphological categories. The integrated  $H\alpha$  luminosity is plotted as a function of the region width  $\sigma$  given by the pseudo-Voigt profile for each region. The different plots outline the different morphology categories (in color), as identified in the right corner, superimposed over the distribution for all the categories (in black). The horizontal dashed line is the luminosity detection limit.

HII regions as a function of the  $\sigma$  value of their pseudo-Voigt fitted profile and their corresponding correlation coefficient. As suspected for the diffuse category, low-luminosity and extended HII regions have a weaker correlation coefficient. Furthermore, Figures 18 and 19 clearly show a lack of extended-high luminosity regions and reveal a possible maximum envelope for a correlation between the compactness and integrated  $H\alpha$  luminosity of the HII regions. Multiple mechanisms could explain this behavior. Firstly, the most massive interstellar clouds are the progenitors of the most luminous regions and these clouds are known to be more dense than the smaller ones (almost a linear function between the mass of the clouds and the ISM density; Morrison MacLachlan 2015). Due to the global equilibrium between the ISM density and the ionizing flux of the source, the high density of these clouds could explain why the massive regions are smaller in size than the low mass, less dense, regions. Secondly, the number of ionizing photons ( $Q_H$ ) emitted by massive stars in the clusters is well constraint by the IMF while more dispersion is observed in low mass clusters where the ionizing stars content reflects a more stochastic sampling of the IMF (Morrison MacLachlan 2015). Additionally, very bright HII regions observed here ( $\log L_{H\alpha} > 38.5$ ) could be density bounded rather than ionization bounded. The latter could also explain their average smaller  $\sigma$  value compared to fainter regions. In the same way, the fainter regions observed (between  $\log L_{H\alpha} = 37$  and  $38.5$ ) can clearly be more extended; Ionization bounded regions in a lower density medium could produce this result.



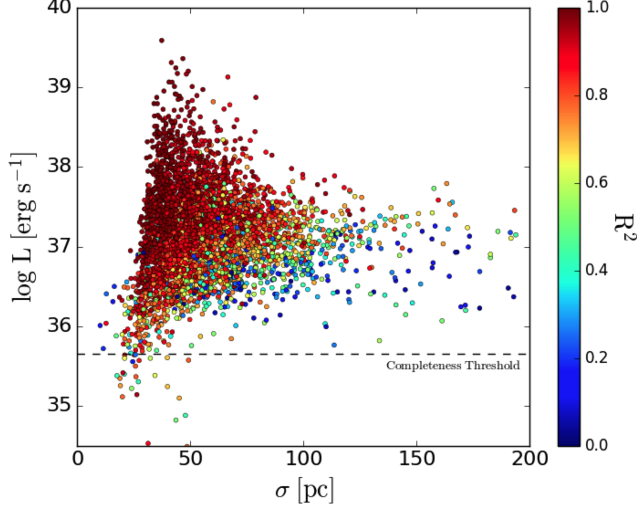


**Figure 19.** The HII regions H $\alpha$  luminosity distribution taking into account the correlation coefficient  $R^2$  for the pseudo-Voigt fitted profile. The integrated H $\alpha$  luminosity is plotted as a function of the region half-width  $\sigma$  given by the pseudo-Voigt fitted profile for each region. Each region is color coded according to  $R^2$ , as indicated to the right. The horizontal dashed line is the luminosity detection limit.

#### 5.4 Size of the HII regions

The size of the HII regions can be compared to spherical models of uniform density (i.e. Strömgren spheres; Osterbrock & Ferland 2006). This spherical model was chosen for its simplicity but is certainly not representative of all of the observed regions (Wood et al. 2005). The radius of a Strömgren sphere is given by :

$$R_S = \frac{3Q_H}{4\pi\epsilon n_e^2 \alpha_B(H, T_e)}, \quad (4)$$

where  $Q_H$  is the number of ionizing photons (with  $E > 13.6$  eV),  $\epsilon$  is the volume filling factor of the ionized gas,  $n_e$  is the electron density, and  $\alpha_B(H, T_e)$  is the recombination coefficient of the hydrogen atom for a given electron temperature ( $T_e$ ). Typical values of  $\epsilon$  for large HII regions are between  $10^{-3}$  and  $10^{-4}$  (according to Giammanco et al. 2004 and Cedrés et al. 2013) and  $\alpha_B(H, 10\,000\text{ K}) = 2.59 \times 10^{-13} \text{ cm}^3 \text{ s}^{-1}$  (Osterbrock 1989). The number of ionizing photons was estimated using the relation given by Morrison MacLachlan (2015):

$$\log(Q_H) = 5.0754 + 42.034x - 15.0797x^2 + 2.4439x^3 - 0.1474x^4, \quad (5)$$

where  $x$  is a function of the cluster stellar mass :  $x = \log(M_{cl}/M_\odot)$ .

To convert the pseudo-Voigt profile half-width  $\sigma$  into a radius, the uniform spherical models intensity profiles were convoluted with a Gaussian to account for differences in image quality and manipulations during data reduction. Then, the H $\alpha$  intensity profile half-width  $\sigma_g$  of the models were obtained by fitting a Gaussian. A relation between  $\sigma_g$  and  $R_S$  was derived and transposed to our measurements to get the corresponding radius  $R_{HII}$ .

Figure 20 shows the HII region integrated H $\alpha$  luminosity as a function of their radius  $R_{HII}$ . Theoretical

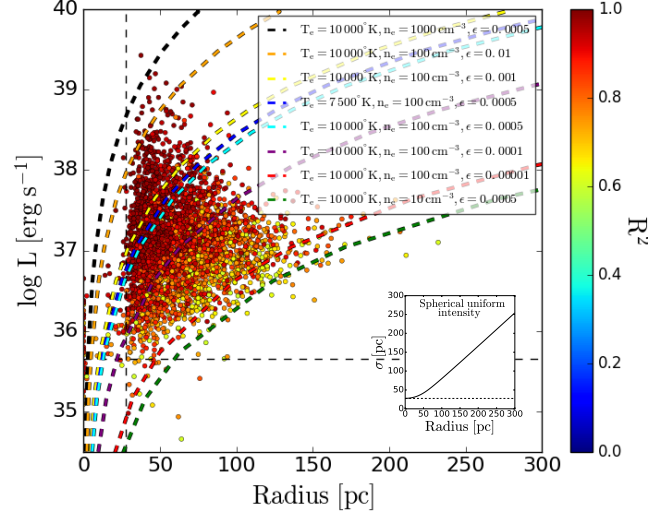


**Figure 20.** The HII regions integrated H $\alpha$  luminosity as a function of their radius  $R_{HII}$  obtained when comparing them with Strömgren spheres. Only regions with a correlation coefficient  $R^2 > 0.6$  are shown. The dashed curves represent the luminosity and radius relation for theoretical Strömgren spheres considering various stellar cluster masses  $M_{cl}$ , electron temperatures  $T_e$  and densities  $n_e$ , and volume filling factors  $\epsilon$ , as indicated in the plot. The vertical dashed line is the sensitivity threshold of the H $\alpha$  intensity distribution for the Strömgren model extracted from the relation between the  $\sigma_g$  of the Gaussian fit for the intensity profile and Strömgren radius  $R_S$  (overplotted in the left lower corner). The horizontal dashed line is the luminosity detection limit.

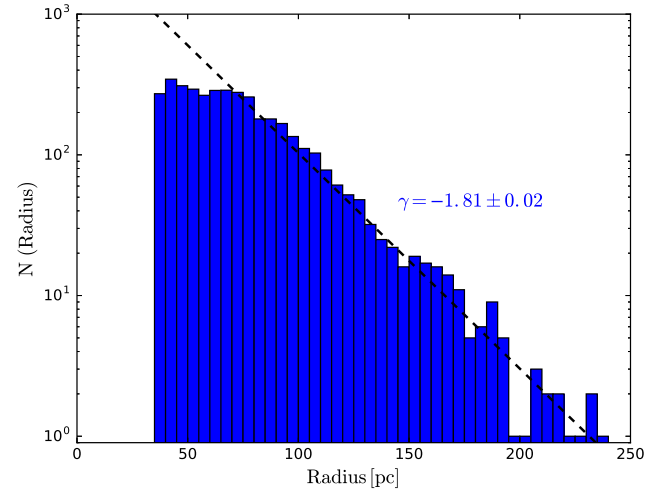


**Figure 21.** Size distribution function of the HII regions. The dashed line shows a linear fit with a slope  $\gamma$  for regions with a radius  $R_{HII}$  between 70 and 250 pc.

curves for Strömgren spheres with various stellar cluster masses, gas electron temperatures and densities, and volume filling factors are included. It is important to note that no luminosity-size relation, such as the often used  $L \propto D^\eta$  (where  $D$  is the diameter), follows the well spread distribution of our measurements. In fact, Scoville et al. (2001), who found  $\eta = 2$ , stated that this relation is biased

by unresolved, superposed, or blended HII regions. Liu et al. (2013) found a value of  $\eta=3$  but also made a careful analysis of the possible misinterpretation of the data, and concluded that the estimation of  $\eta$  is strongly affected either by the algorithm used to define the regions or by observational biases. Here, the combination of the good spatial resolution, our HII region identification technique, and radius definition method reveal the complex nature of the luminosity-size distribution of NGC 628 HII regions. Multiple models for different ISM conditions are required to understand this distribution. From the comparison with the theoretical curves, we can see that the electron temperature has a very small effect on the HII region radius, whereas both the electron density and the volume filling factor can be hold responsible for most of the scattering. Also, as the size of a bright HII region increases, the electron density and/or the volume filling factor decreases. From the general distribution of the low-luminosity regions and the models, we can conclude that they are either dense and small, with a higher electron density and volume filling factor, or (most probably) diffuse and large, with a smaller electron density and volume filling factor in agreement with the fact that low-mass HII regions are less dense and ionization bounded. For bright regions, the size is globally smaller (between 30 and 100 pc) in comparison with the low-luminosity sample. The bright HII regions have either a high electron density and/or a high volume filling factor.

Figure 21 shows the size distribution function of the HII regions. It follows the relation  $N(R_{HII})dR_{HII} = AR_{HII}^{-\gamma}dR_{HII}$ , where  $N(R_{HII})dR_{HII}$  is the number of HII regions with radius in the range  $R_{HII}$  to  $R_{HII}+dR_{HII}$ . The ability to recover the size of a region is limited by the spatial resolution of the data and the physical distance between regions. Therefore, the measured size of the smallest regions is only an upper limit. The slopes  $\gamma = 1.81 \pm 0.02$ , obtained between 70 and 250 pc, is in good agreement with previous investigations in nearby galaxies (for example, Gusev 2014 found a value between 1.75 and 2.5 for regions between 50 and 170 pc).

## 6 LINE RATIOS OF THE HII REGIONS

### 6.1 Line Ratios for Individual Spaxel

Line ratios were calculated using flux maps of the lines extracted with ORCS (§ 3.5). Line ratios of  $[OII]/[NII]$ ,  $[OIII]/[NII]$ ,  $[OIII]/[OII]$ ,  $[OII]/H\beta$ ,  $([OII]+[OIII])/H\beta$ ,  $[NII]/H\alpha$ ,  $[SII]/H\alpha$ ,  $[SII]/[NII]$ ,  $[OIII]/H\beta$ , and  $[SII]\lambda 6716/[SII]\lambda 6731$  were obtained after extinction correction. Appendix B contains line ratio maps covering the whole galaxy as well as for four enlarged reference sections of the disc. A detection threshold of  $3\sigma$  for the individual lines was applied to produce these maps. The maps of the four enlarged reference sections are really useful variations of the line ratios within HII regions themselves (the  $H\alpha$  emission peaks are all indicated with a cross on the images) and the DIG. For example, in Figure B1, that the  $\log [NII]/H\alpha$  ratio can change significantly within a distance of 100 pc. The position of the maximum can be superimposed to low-or high-local values of the ratio and large fluctuations can be seen in the DIG surrounding the

peaks. Also, in the case of the  $\log [SII]/H\alpha$  ratio (Fig. B3), there is a strong correlation between the position of the peaks and local minimum values. This behavior is expected as this ratio is known to increase when the DIG contribution is important. Figure 22 shows the BPT diagram (as initially defined by Baldwin et al. 1981) of  $[OIII]/H\beta$  vs  $[NII]/H\alpha$  for all the spaxels measured over the whole galaxy disc. Two versions of the same diagram are shown, one color coded according to the  $H\alpha$  flux for each spaxel and the other according to the spaxel density. As expected, most spaxels lie in the HII region ionization regime area of the BPT diagram and a few spaxels cross the transition zone and AGN limit. The general trend drawn by the bright  $H\alpha$  spaxels (red curve in the Fig. 22) can be represented by the polynomial fit :

$$\log ([NII]/H\alpha) = -0.6841 - 0.651x - 0.9026x^2 - 0.4249x^3 - 0.06401x^4, \quad (6)$$

where  $x = \log([OIII]/H\beta)$ . Globally, the fit (going from high to low  $[OIII]/H\beta$  ratio) follows an increase in the gas metallicity. We can also notice a turnover at  $\log([OIII]/H\beta) = -0.5$  and  $\log([NII]/H\alpha) = -0.5$ , where the  $[NII]/H\alpha$  ratio starts to decrease while the  $[OIII]/H\beta$  continues to decrease. This turnover is expected when the metallicity reaches a value above  $\log[O/H] \simeq 9$  (Fig. 7 from Kewley & Dopita 2002) while considering that the number of ionizing photons and therefore the ionization parameter ( $q = Q_H/n_H$ , the number of hydrogen ionizing photons over the hydrogen atom density) both decrease with increasing metallicity (number of ionizing photons as a function of the metallicity; Topping & Shull 2015, or ionization parameter as a function of the metallicity; Pérez-Montero et al. 2014). A turnover may also be due to a variation in the relative abundances (e.g. N/O) in the galaxy. Therefore, the location of the polynomial fit and the possible turnover are expected to vary for galaxies with different metallicities, relative abundances, and properties.

In Figure 22, the spaxels that are bright in  $H\alpha$  are predominantly associated to massive HII regions, where it is most likely that the IMF is well represented (i.e. no stochastic sampling with the theoretical slope and mass limits). The dispersion observed along the fit in the bright  $H\alpha$  spaxels could therefore be mainly attributed to different ages (as the ionizing spectrum gets less energetic with time with the death of the most massive stars). On the contrary, the dispersion of faint  $H\alpha$  spaxels can be due to multiple causes : age, IMF under-sampling, DIG contamination, different sources of ionization, SNR, etc.

In the right panel of Figure 22, the density envelop of the BPT diagram shows two peaks. The extended structure associated to the most intense peak is correlated with the maximum of the  $[NII]/H\alpha$  ratio (around  $[-0.5, -0.5]$ ). The structure associated to the less intense peak (around  $[-0.8, 0.2]$ ) seems to be correlated with the position where the spaxels diverge toward the transition and AGN zones, suggesting ionizing sources that are different from young stellar clusters.

Figure 23 shows the  $[OIII]/H\beta$  vs  $[NII]/H\alpha$  BPT diagram by taking into account the spaxel distance to its ionizing source (i.e. the distance between the spaxel and the emission peak within the zone of influence defining an HII region). Diagrams are displayed independently for very

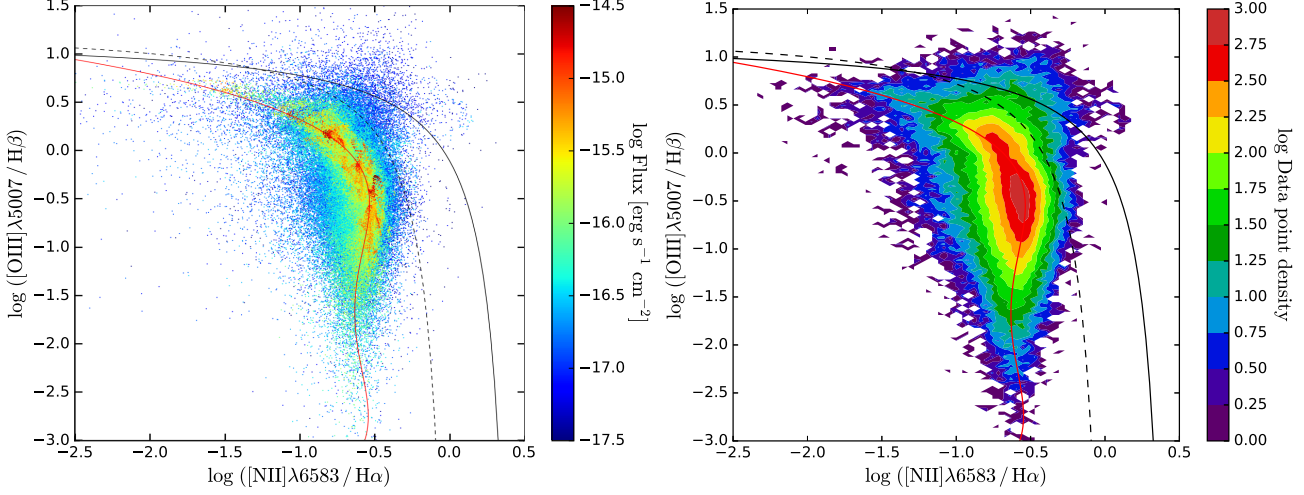


**Figure 22.** BPT diagram of  $[\text{OIII}]/\text{H}\beta$  vs  $[\text{NII}]/\text{H}\alpha$  for all the spaxels measured, on the left, color coded according to their  $\text{H}\alpha$  flux, and on the right, color coded according to the spaxel density. The dashed line defines the BPT limit between the HII regions and the transition zone, whereas the black line defines the BPT limit between the transition zone and the AGN regime. The red line corresponds to the polynomial fit of the data. In the left panel, spaxel values are stacked over each other from the faintest  $\text{H}\alpha$  flux region to the brightest one, and therefore, bright spaxels always appear in front.

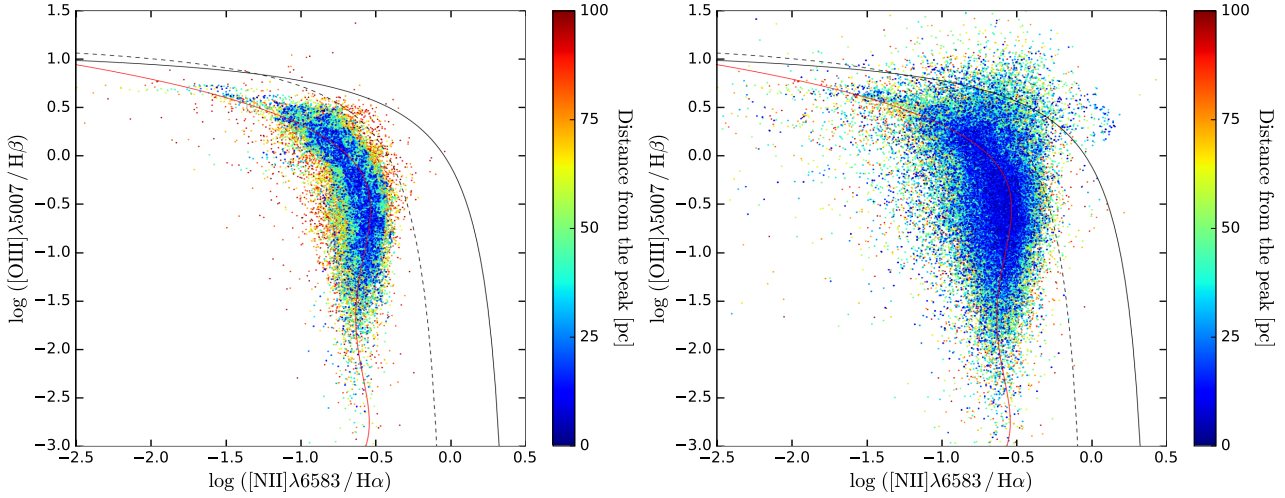


**Figure 23.** BPT diagram of  $[\text{OIII}]/\text{H}\beta$  vs  $[\text{NII}]/\text{H}\alpha$  for spaxels included in very bright HII regions (i.e. regions with an integrated  $\text{H}\alpha$  flux above  $5 \times 10^{-15} \text{ erg s}^{-1} \text{ cm}^{-2}$ ; on the left) and, for moderately bright spaxels (i.e. spaxels with an  $\text{H}\alpha$  flux above  $5 \times 10^{-16} \text{ erg s}^{-1} \text{ cm}^{-2}$ ; on the right). The plots are color coded according to the spaxel distance to its emission peak. Spaxel values are stacked over each other from the more distant to the closest one, and therefore, closest regions always appear in front. The curves are as in Figure 22.

bright HII regions (i.e. with an integrated  $\text{H}\alpha$  flux above  $5 \times 10^{-15} \text{ erg s}^{-1} \text{ cm}^{-2}$ ) and for moderately bright spaxels (i.e. with an integrated  $\text{H}\alpha$  flux above  $5 \times 10^{-16} \text{ erg s}^{-1} \text{ cm}^{-2}$ ). In the case of very bright HII regions (Fig. 23 left panel), the further away they are from their emission peak, the greater is the dispersion around the best polynomial fit. In the case of the sample including moderately bright HII regions (Fig. 23 right panel), the relation with the distance to the emission peak is more ambiguous. In this case, for moderately bright regions, the effect of the distance is mixed with other parameters like the age, IMF under-sampling, DIG contribution, and other sources of ionization, as seen in the previous paragraph for less massive HII regions.

Figure 24 shows the  $[\text{OIII}]/\text{H}\beta$  vs  $[\text{NII}]/\text{H}\alpha$  BTP dia-

gram as a function of the spaxel galactocentric radius  $R_G$ , for bright regions and moderately bright regions. The general distribution of the colors in these plots reflects the metallicity gradient of the galaxy. The central spaxels (in blue) are more metal rich than those of the extended disc (in yellow-orange-red), as they have larger values of  $[\text{NII}]/\text{H}\alpha$  and smaller values of  $[\text{OIII}]/\text{H}\beta$  (as expected from the global metallicity indicators, e.g. Pettini & Pagel 2004). Nevertheless, the northern spiral arm, located at a distance larger than 15 kpc (red dots in the plots near  $\log([\text{OIII}]/\text{H}\beta) \simeq 0$ ), behaves differently than this somewhat traditional linear-negative metallicity gradient. This could be due to a flattening or an inversion of the slope of the metallicity gradient at large galactocentric radius and/or to a change in the



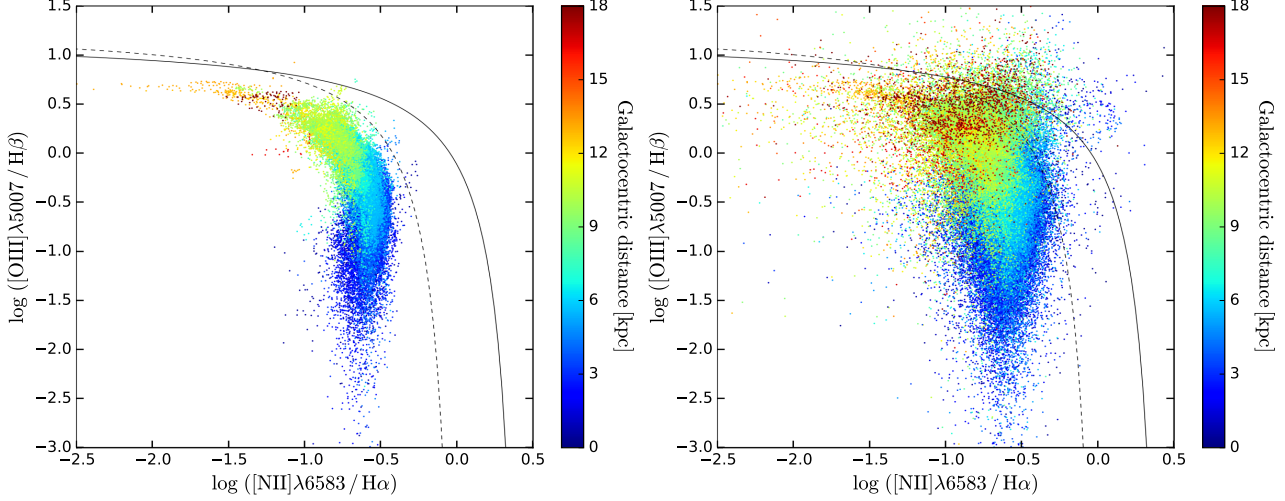


**Figure 24.** BPT diagram of  $[\text{OIII}]/\text{H}\beta$  vs  $[\text{NII}]/\text{H}\alpha$  for spaxels included in very bright HII regions (i.e. regions with an integrated  $\text{H}\alpha$  flux above  $5 \times 10^{-15} \text{ erg s}^{-1} \text{ cm}^{-2}$ ; on the left), and for moderately bright spaxels (i.e. spaxels with an  $\text{H}\alpha$  flux above  $5 \times 10^{-17} \text{ erg s}^{-1} \text{ cm}^{-2}$ ; on the right). The plots are color coded according to the spaxel galactocentric radius  $R_{\text{gla}}$ . Spaxel values are stacked over each other from the smallest radius to the larger one, and therefore, spaxels at large radius always appear in front. The curves are as in Figure 22.

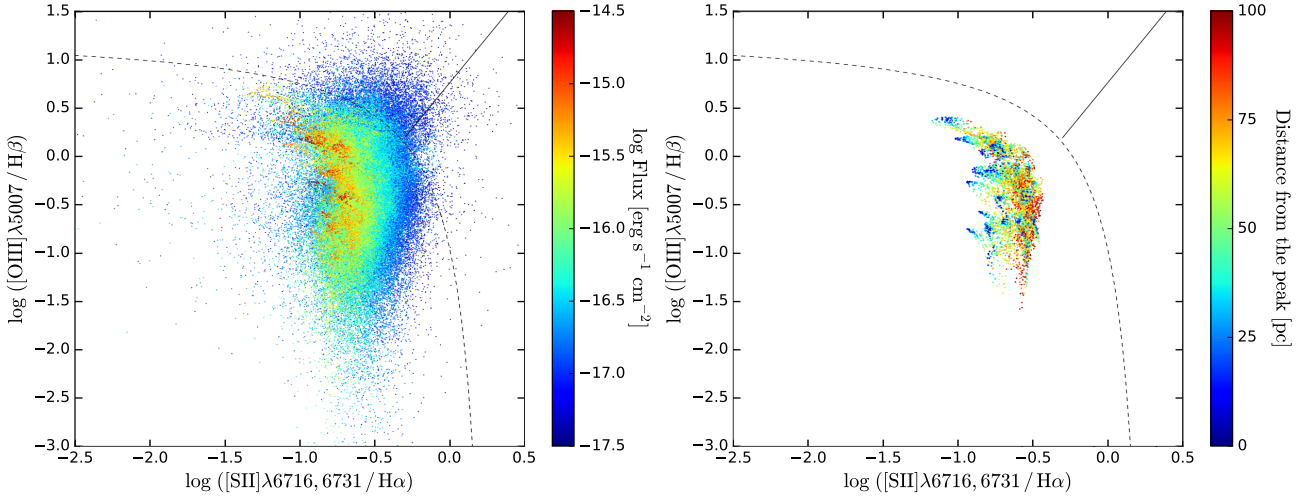


**Figure 25.** BPT diagram of  $[\text{OIII}]/\text{H}\beta$  vs  $[\text{SII}]/\text{H}\alpha$  for all spaxels measured color coded according to their  $\text{H}\alpha$  intensity (to the left), and, for spaxels from extremely bright HII regions (integrated  $\text{H}\alpha$  flux above  $3 \times 10^{-14} \text{ erg s}^{-1} \text{ cm}^{-2}$ ) color coded according to the spaxel distance to the emission peak (to the right). The dashed line defines the BPT limit between the HII regions and the AGN ionization regime, whereas the full line defines the BPT limit between the Seyfert and LINER ionization regime. On the left, spaxel values are stacked over each other from the faintest  $\text{H}\alpha$  flux to the brightest one, and therefore, bright spaxels always appear in front. On the right, spaxel values are stacked over each other from the more distant to the closest one, and therefore, closest regions always appear in front.

gradient of the relative abundance of N/O.

Figure 25 shows the  $[\text{OIII}]/\text{H}\beta$  vs  $[\text{SII}]/\text{H}\alpha$  BTP diagram for all the spaxels measured, while taking into account the  $\text{H}\alpha$  flux and the distance to the emission peak. Again the spaxels from the brightest HII regions are found within the HII region ionization regime. Those closer to the emission peak display a smaller  $[\text{SII}]/\text{H}\alpha$  ratio in general. Larger values for this ratio are a signature of DIG (Kreckel et al. 2016).

## 6.2 Line Ratios for Each Region

For each region detected from the  $\text{H}\alpha$  flux, as described in Section 4, global line ratios were evaluated by fitting the integrated flux that is encompassed within an aperture radius corresponding to the half-width  $\sigma$  of the region pseudo-Voigt fitted intensity profile. We selected the half-width  $\sigma$  of the region pseudo-Voigt fitted intensity profile instead of the regions outer limit in order to minimize the DIG contribution to the integrated spectrum. All lines in the integrated spectrum of each region were fitted using ORCS as described in Section 3. Figure 26 shows the BPT diagrams of  $[\text{OIII}]/\text{H}\beta$  vs  $[\text{NII}]/\text{H}\alpha$ ,  $[\text{OIII}]/\text{H}\beta$  vs  $[\text{SII}]/\text{H}\alpha$ ,  $[\text{OIII}]/\text{H}\beta$  vs  $[\text{OII}]/\text{H}\beta$ ,

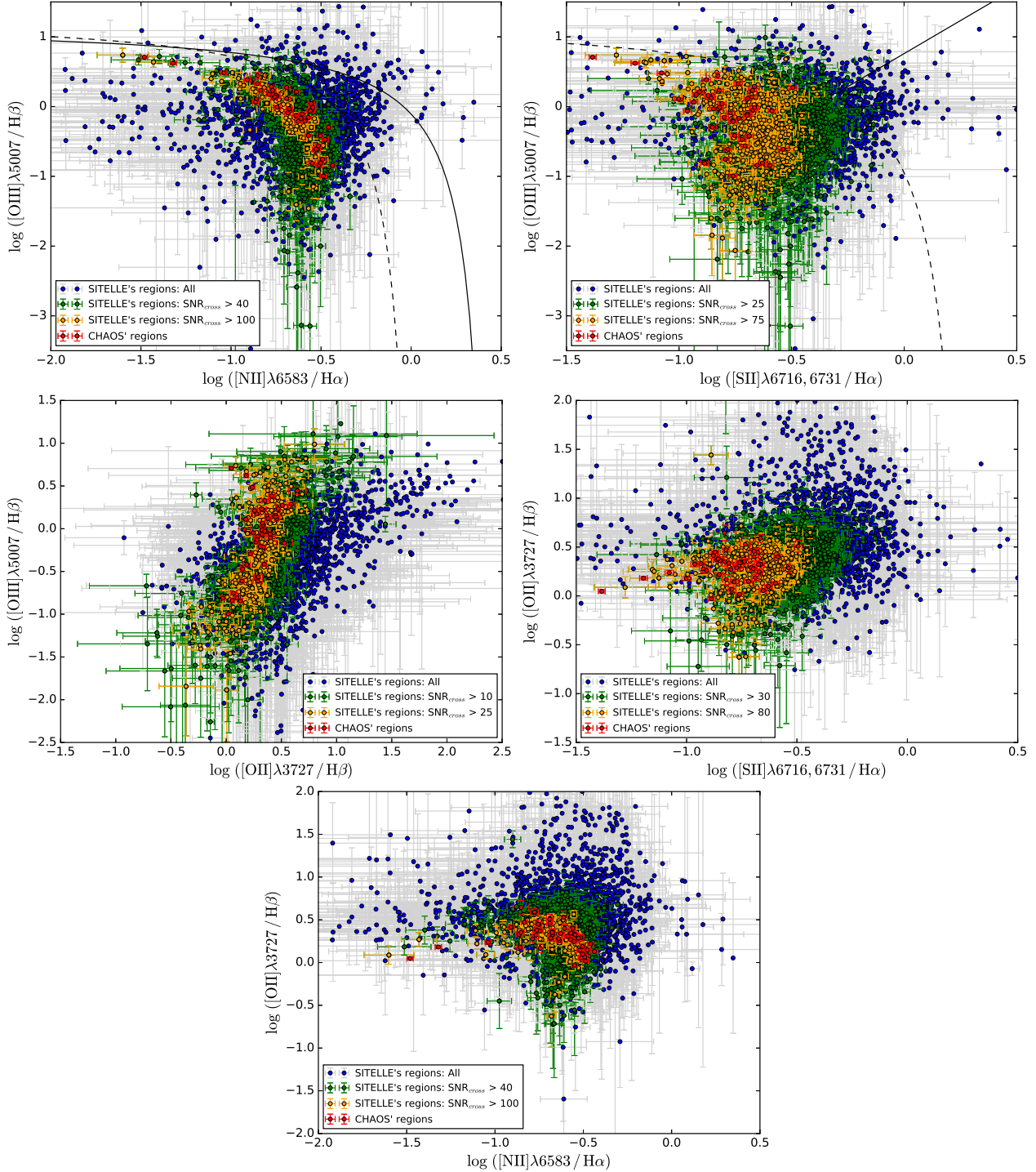


**Figure 26.** BPT diagrams of  $[\text{OIII}]/\text{H}\beta$  vs  $[\text{NII}]/\text{H}\alpha$ ,  $[\text{OIII}]/\text{H}\beta$  vs  $[\text{SII}]/\text{H}\alpha$ ,  $[\text{OIII}]/\text{H}\beta$  vs  $[\text{OII}]/\text{H}\beta$ ,  $[\text{OII}]/\text{H}\beta$  vs  $[\text{SII}]/\text{H}\alpha$ , and  $[\text{OII}]/\text{H}\beta$  vs  $[\text{NII}]/\text{H}\alpha$  based on the integrated spectra of each region identified with SITELLE. Blue dots with gray error bars are for line ratios where all the lines have an  $\text{SNR} > 3$ . Green and orange symbols identify line ratios with  $\text{SNR}_{\text{cross}}$  greater than the two selected thresholds. The regions observed for the CHAOS project by Berg et al. (2015) are plotted in red. Black curves in the top panels are as in Figures 22 and 25.

$[\text{OII}]/\text{H}\beta$  vs  $[\text{SII}]/\text{H}\alpha$ , and  $[\text{OII}]/\text{H}\beta$  vs  $[\text{NII}]/\text{H}\alpha$  separating the regions according to the SNR. Three different SNR thresholds have been considered. All the lines used in a diagram must have an  $\text{SNR} > 3$ , and at least one line among those used in a diagram must have a  $\text{SNR}_{\text{cross}}$  greater than

two selected thresholds that depend on the line ratio selected (for values see the caption of Fig. 26). The bright HII regions from the CHAOS project (Berg et al. 2015) are also shown in our diagrams.

Again, most regions identified fall in the ionizing zone

for the HII regions. The comparison with the CHAOS sample, where only the highest  $H\alpha$  surface brightness knots have been selected (Berg et al. 2015), demonstrates SITELLE’s ability to reproduce line ratios previously observed for these regions, i.e. the CHAOS data are well superimposed to the SITELLEs regions with the highest  $SNR_{cross}$  threshold selected. As these bright regions probably represent the most massive and youngest HII regions, our larger sample includes objects with a wider range of physical properties (masses, ages, stellar content, ISM properties, etc.) allowing us to see an unbiased distribution in the BPT diagrams. The Appendix B also presents plots of line ratios as a function of the galactocentric radius.

SITELLE and CHAOS samples show a good agreement for all the other line ratios. The dispersion observed is different as the CHAOS sample includes only the brightest HII regions. There is, however, a clear discrepancy between SITELLE and CHAOS for the trend seen when the [SII] lines are included. These lines are very sensitive to the DIG (Haffner et al. 1999; Elwert & Dettmar 2005) and we suspect that the difference observed could be either related to the subtraction of the DIG background in the CHAOS data processing technique or the selection bias. Indeed, Berg et al. (2015) mention a sky subtraction using a 2D background fit within the slit used to observe an HII region; this background may include a significant contribution for the DIG. In our case we measured the line ratios using a limited aperture on the half-width  $\sigma$  of the region pseudo-Voigt fitted intensity profile to minimize the DIG without doing any subtraction. But, it could also be due to the selection bias, as bright regions (with high ionization parameter) are more likely to present low [SII]/ $H\alpha$  ratios.

## 7 SUMMARY

In this first paper of a larger program focusing on star formation and chemical evolution in disc galaxies, we have shown the high potential of SITELLE for the study of nearby extragalactic HII regions from observations on the well-known spiral NGC 628. Our results are as follows:

- 1) From our datacubes covering the whole disc of NGC 628, we identified 4285 HII region candidates. Ten strong and semi-strong emission lines have been sampled in about 4 billion spaxels using automated routines specifically created for SITELLE. We developed a new identification procedure for the regions, i.e. to find out all the emission peaks and define their zone of influence. Using both the spatial and spectral information, this new procedure optimizes the number of parameters extracted for each region (RA/DEC position, dust extinction, velocity,  $H\alpha$  profile, DIG background, luminosity, size, morphological type, integrated line fluxes, etc.).

- 2) By comparing the intensity profile of the regions, four morphological categories, from spherical to diffuse, were defined. These morphologies point out to different types of stellar aggregates (dense or sparse) and different gas distributions (homogeneous to filamentary).

- 3) A well-sampled luminosity function of the HII regions was obtained and we studied its variation as a function of the location of the regions along the galactic radius and the DIG background flux. Using the complete sample, a con-

stant slope of  $\alpha_{cor} = -1.12 \pm 0.03$  (corrected for the dust extinction, using the Balmer lines, and for the galaxy disc stellar populations on the line of sight to each HII region) was found; no evidence of a break in the distribution was noticed. The slope remains the same while selecting subsample of regions located at different galactic radius (which can be seen as different metallicity range). A significant change of the slope is seen when considering only regions with a low DIG background. We noticed that high DIG regions are close or belong to the spiral arms of the galaxy (in agreement with the findings of Kreckel et al. 2016). A correlation between the DIG background flux and the total  $H\alpha$  luminosity of the bright regions was found, suggesting that ionizing photons primarily related to massive stars and escaping directly from these regions are the main source for the DIG. We also showed that the global DIG background (in fainter regions outside the spiral arms) increases slowly toward the galaxy center. This behavior rather points to an additional source for the DIG ionization related to evolved stars, as these are more numerous closer to the galaxy center.

- 4) The high spatial resolution of SITELLE allowed us to compare the integrated  $H\alpha$  luminosity of the regions with their intensity profile width (i.e.  $\sigma$  of a pseudo-Voigt fit). Diffused/extended high luminosity regions are not seen while low luminosity regions present a wide range of compactness. This is in agreement with the proposition that denser clouds are the progenitors of the most massive HII regions (Morrison MacLachlan 2015) and the fact that massive regions are density bounded rather than ionization bounded. In less massive HII regions, the number of ionizing photons is subject to IMF fluctuations and the Strömgren radius of regions in a lower density medium is ionization bounded. Therefore low luminosity HII regions present a wider range in size.

- 5) The size of the regions was evaluated using the  $H\alpha$  profile and a simple Strömgren sphere model. The size distribution function (i.e. number of regions versus their radius) shows a well defined slope  $\gamma = 1.81 \pm 0.02$  for radii between 70 to 250 pc, as found from other studies.

- 6) We looked at the distribution of the line ratios for the individual spaxels and for the integrated regions in different BPT diagrams. Bright spaxels show a distinct turnover in the [OIII]/ $H\beta$  vs [NII]/ $H\alpha$  diagram. A larger dispersion is seen for the fainter  $H\alpha$  spaxels which can be due to their age, IMF under-sampling, DIG contamination, different sources of ionization, SNR, etc. High-definition maps of the line ratios reveal the complex variations of the ionization conditions within the HII regions themselves. A polynomial fit of each line ratios as a function of the galactocentric radius is now available for comparative studies.

- 6) And finally, detailed information on the emission line regions of NGC 628 have been extracted from the SITELLE data. We have consolidated the information for all the 4285 regions identified in a catalog.

Table 3 shows an example of the catalog content. The objective of this new catalog is to provide a complete database to study the vast parameter space covered by star-forming regions. Further work on NGC 628 will address HII region characteristics and nebular physics (abundances, mass, age, ionization parameter, density) in a more detailed manner. In the following paper, we will use photoionization models to investigate the ionization conditions in the HII regions of NGC 628.

## ACKNOWLEDGMENTS

This research is based on observations obtained at the Canada-France-Hawaii Telescope (CFHT) which is operated from the summit of Maunakea by the National Research Council of Canada, the Institut National des Sciences de l'Univers of the Centre National de la Recherche Scientifique of France, and the University of Hawaii. The observations at the Canada-France-Hawaii Telescope were performed with care and respect from the summit of Maunakea which is a significant cultural and historic site. The observations were obtained with SITELE, a joint project between Université Laval, ABB-Bomem, Université de Montréal and the CFHT with funding support from the Canada Foundation for Innovation (CFI), the National Sciences and Engineering Research Council of Canada (NSERC), Fonds de Recherche du Québec - Nature et Technologies (FRQNT), and CFHT.

LRN, CR, and LD are grateful to the Fonds de recherche du Québec - Nature et Technologies (FRQNT) for individual and team financial support. LD thanks the Canada Research Chair program. CR and LD are grateful to the Natural Sciences and Engineering Research Council of Canada (NSERC). This research has made use of NASA's Astrophysics Data System and of the VizieR catalogue access tool, CDS, Strasbourg, France.

## REFERENCES

- Allen, M. G., Groves, B. A., Dopita, M. A., Sutherland, R. S. & Kewley, L. J. 2008, *ApJS*, 178, 20
- Azimlu, M., Marciniak, R., & Barmby, P. 2011, *AJ*, 142, 139A
- Baldwin, J. A., Phillips, M. M., & Terlevich, R. 1981, *PASP*, 93 5
- Berg, D. A. et al. 2015, *ApJ*, 806, 16
- Blanc, G. A., Heiderman, A., Gebhardt, K., Evans, N. J., & Adams, J. 2009, *ApJ*, 704, 842
- Bradley, T. R., Knapen, J. H., Beckman, J. E. & Folkes, S. L. 2006, *A&A* 459, 13
- Cardelli, J. A., Clayton G. C. & Mathis J. S. 1989, *ApJ*, 345, 245
- Cedr s, B. et al. 2013, *ApJ*, 765, 24
- Davies, R. L., Kewley, L.J., Ho, I. & Dopita, M. A. 2014, *MNRAS*, 444 3961
- Drissen, L., Rousseau-Nepton, L., Lavoie, S., Robert, C., Martin, T., Martin, P., Mandar, J. & Grandmont, F. 2014, *Advances in Astronomy*, 2014, 293856
- Elwert, T. & Dettmar, R.-J. 2005, *ASP*, 331, 203
- Ferland, G. J., Korista, K. T., Verner, D. A., Ferguson, J. W., Kingdon, J. B., & Verner, E. M. 1998, *PASP*, 110, 761
- Flores-Fajardo, N., Morisset, C., Stas nska, G. & Binette, L. 2011, *MNRAS*, 415, 2182
- Kewley, L. J. & Dopita, M. A. 2002, *ApJS*, 142, 35
- Kreckel, K., Blanc, G. A., Groves, B., Adamo, A., Hughes, A., & Meidt, S. 2016, *arXiv160308009K*
- Giammanco, C., Beckman, J. E., Zurita, A., & Rela o, M. 2004, *A&A* 424, 877
- Grasha, K. et al. 2015, *ApJ*, 815, 93
- Gusev, A. S. 2014, *MNRAS*, 442, 3711
- Haffner, L. M., Reynolds, R. J. & Tufte, S. L. 1999, *ApJ*, 523, 223
- Ho, L. C. 2008, *RA & A*, 76
- Liu, G., Calzetti, D. Kennicutt, R. C. Jr., Schinnerer, E., Sofue, Y., Komugi, S., Egusa, F., & Scoville, N. Z. 2013, *ApJ*, 772, 27
- Martin T. 2015, PhD Thesis, Universit  Laval, Canada
- Martin, T., Drissen, L., & Joncas, G. 2015, *ASP Conf. serie: ADASS XXIV*, 495, 327
- Martin, T. B., Prunet, S., & Drissen, L. 2016, *MNRAS*, 463, 4223
- Martin, T. & Drissen, L., 2016, *Proc. FSA & October*, 23
- Mast, D. et al. 2014, *A&A*, 561,129
- McCall, M. , Straker, R. W., & Uomoto, A. K. 1996, *AJ*, 112, 1096
- Moll , M., Garc a-Vargas, M. L. & Bressan, A. 2009, *MNRAS*, 398, 451
- Morisset, C., Delgado-Inglada, G., & Flores-Fajardo, N. 2015, *RMA&A*, 51,108
- Morrison MacLachlan, J. 2015, PhD Thesis, University of St Andrews
- Nelder, J. & Mead, R. 1965, *Computer Journal* Vol. 7, 4, 308
- Nicholls, D. C., Dopita, M. A., Sutherland, R. S., Kewley, L. J. & Palay, E. 2013, *ApJS*, 207, 21
- Osterbrock, D. E. 1989, *Astrophysics of gaseous nebulae and active galactic nuclei*
- Osterbrock, D. E. & Ferland, G. J. 2006, *Astrophysics of gaseous nebulae and active galactic nuclei (2nd Edition)*
- O'Dell, C. R., Ferland, & G. J., Peimbert, M. 2017, *MNRAS*, 464, 4835
- Pettini M. & Pagel B. E. J. 2004, *MNRAS*, 348, L59
- P rez-Montero, E., Monreal-Ibero, A., Relano, M., V lchez, J. M., Kehrig, C. & Morisset, C. 2014, *A&A* 566, A12
- Pilyugin, L. S., Grebel, E. K. & Kniazev, A. Y. 2014 *AJ*, 147, 131
- Rosales-Ortega, F. F., Diaz, A. I., Kennicutt, R. C., & S nchez, S. F. 2011, *MNRAS*, 415, 2439
- Rousseau-Nepton, L. 2017, Th se de Doctorat, Universit  Laval
- S nchez, S. F., Rosales-Ortega, F. F., Kennicutt, R. C., Johnson, B. D., Diaz, A. I., Pasquali, A., & Hao, C. N. 2011, *MNRAS*, 410, 313
- Scoville, N. Z., Polletta, M., Ewald, S., Stolovy, S. R., Thompson, R. & Rieke, M. 2001, *ApJ*, 122, 3017
- Shara, M. M., Drissen, L., Martin, T., Alarie, A., & Stephenson, F. R. 2016, *MNRAS*, 465, 739
- Sutherland, R. S. & Dopita, M. A. 1993, *ApJS*, 88, 253
- Thilker, D. A., Braun, R., & Walterbos, R. A. M. 2000, *ApJ*, 120, 3070
- Thilker, D. A., Walterbos, R. A. M., Braun, R., & Hoopes, C. G. 2002, *ApJ*, 124, 3118
- Topping, M. W. & Shull, J. M. 2015, *ApJ*, 800, 97
- Vale Asar, N., Wild, V., Kennicutt, R. C., & Cid Fernandes, R. 2014, *RMA&A*, 44, 91
- Villaverde, M., Cervi o, M., & Luridiana, V. 2010, *A&A*, 522, 49
- Wood, K., Haffner, L. M., Reynolds, R. J., Mathis, J. S., & Madsen, G. 2005, *ApJ*, 633, 295W
- Yuan, T.-T., Kewley, L. J. & Rich, J. 2013, *ApJ*, 767,106



**Table 3.** Catalog Parameters

ID	RA	DEC	$R_G$	$\text{Log } L_{H\alpha}$	$\text{log DIG}_{SB}$	Cat	$I0_{profile}$	$A_{profile}$	$\sigma_{profile}$	$\alpha_{profile}$	$R^2_{profile}$	Size	E(B–V)	$E(B-V)_{err}$
#	–	–	kpc	–	$\text{erg s}^{-1} \text{cm}^{-2} \text{spaxel}^{-1}$	#	$\text{erg s}^{-1} \text{cm}^{-2}$	$\text{erg s}^{-1} \text{cm}^{-2}$	pc	%	–	pc	mag	±
2430	24.1818	15.7876	1.39	37.20	-17.26	1	-15.89	-14.22	39.34	0.72	0.96	46.0	0.408	0.172
2431	24.1375	15.7867	5.48	37.21	-16.85	3	-15.87	-13.92	64.66	0.50	0.95	64.3	0.227	0.048
2432	24.1368	15.7868	4.60	36.49	-17.65	2	-16.92	-14.84	84.41	0.44	0.51	84.2	1.265	0.090
2433	24.2040	15.7882	3.89	37.10	-16.91	3	-16.33	-14.34	77.23	0.60	0.62	97.0	0.347	0.147
2434	24.1891	15.7879	0.83	37.87	-17.06	3	-15.38	-13.61	43.87	0.50	0.96	43.7	0.356	0.053
2435	24.1773	15.7876	5.64	37.70	-16.89	2	-15.49	-13.54	65.68	0.50	0.95	83.0	0.286	0.029
2436	24.2416	15.7892	10.28	37.22	-17.36	1	-15.95	-14.21	40.61	0.50	0.97	48.0	0.308	0.057
2437	24.2121	15.7885	5.82	38.63	-16.72	1	-14.46	-12.79	34.29	0.50	0.99	35.0	0.349	0.026
2438	24.2021	15.7883	4.31	37.35	-17.81	3	-16.02	-14.25	59.17	1.00	0.87	75.0	0.479	0.275
2439	24.1997	15.7881	4.06	37.06	-17.34	3	-16.40	-14.21	114.01	0.48	0.30	140.0	0.000	0.091
2440	24.1990	15.7881	2.52	37.04	-17.45	3	-16.09	-14.39	44.32	0.77	0.84	54.00	0.261	0.188
2441	24.1959	15.7881	1.68	37.28	-17.28	3	-16.23	-14.08	102.78	0.50	0.44	127.00	0.067	0.168
2442	24.1840	15.7878	0.67	–	–	4	-16.61	-14.70	60.00	0.50	0.00	76.00	0.607	0.994
2443	24.1736	15.7876	0.79	37.45	-16.89	3	-15.64	-13.82	48.25	0.50	0.92	60.00	0.448	0.080
2444	24.1702	15.7876	0.91	37.06	-17.26	4	-16.51	-14.48	79.00	0.50	0.48	99.00	0.000	0.212
2445	24.1630	15.7874	1.68	36.67	-17.51	4	-16.47	-14.48	72.77	0.50	0.86	72.45	1.154	0.708
...	...	...	...	...	...	...	...	...	...	...	...	...	...	...

$\text{log} ([\text{NII}]/\text{H}\alpha)$	$\text{log} ([\text{NII}]/\text{H}\alpha)_{err}$	$\text{log} ([\text{NII}]/\text{H}\alpha) \text{SNR}_{cross}$	$\text{log} ([\text{SII}]/\text{H}\alpha)$	$\text{log} ([\text{SII}]/\text{H}\alpha)_{err}$	$\text{log} ([\text{SII}]/\text{H}\alpha) \text{SNR}_{cross}$	...*
–	±	–	–	±	–	...
-0.450	0.069	20.919	-0.657	0.114	20.919	...
-0.629	0.023	56.179	-0.615	0.042	56.179	...
-0.898	0.162	8.021	-0.413	0.329	8.021	...
-0.487	0.048	29.180	-0.452	0.086	29.180	...
-0.597	0.024	54.618	-0.768	0.042	54.618	...
-0.618	0.014	88.427	-0.627	0.026	88.427	...
-0.769	0.023	52.319	-0.504	0.047	52.319	...
-0.586	0.017	77.199	-0.696	0.030	77.199	...
-0.592	0.069	19.538	-0.443	0.130	19.538	...
-0.493	0.056	25.023	-0.396	0.104	25.023	...
-0.698	0.067	19.171	-0.444	0.133	19.171	...
-0.610	0.061	21.629	-0.505	0.117	21.629	...
-0.330	0.302	5.915	0.034	0.631	6.344	...
-0.461	0.035	40.596	-0.801	0.056	40.596	...
-0.109	0.182	10.803	-0.213	0.274	10.803	...
-0.243	0.178	9.849	-0.201	0.400	9.849	...
...	...	...	...	...	...	...

\*All line ratios listed in Section 6.2 are included in the catalog.  
Note: More parameters can be provided upon request.

**APPENDIX A: VELOCITY AND FLUX MAPS**

The velocity map in Figure A1 was produced after a refinement of the wavelength calibration of the SN3 datacube using a sky line (§ 3.1). All the emission lines from this high-spectral resolution datacube have been used simultaneously to extract the velocity in each spaxel individually using the line fitting routine from ORCS (§ 3.5). All the spaxels with  $\text{SNR}_{H\alpha} > 3$  have been kept for this figure.

The flux map for all the emission lines seen in the three filters are shown in Figures A2 and A3. Emission lines from the same filter have been fitted simultaneously using the routine from ORCS § 3.5) applied to all the spaxels individually. The subtraction of the galaxy stellar population spectrum on the line of sight for each spaxels was done (§ 3.4). The correction for the internal extinction has not been applied for these figures. For these figures, all spaxels have been kept regardless of the SNR measured for the lines.

**APPENDIX B: LINE RATIOS**

Appendix B contains the line ratio maps covering the whole galaxy and the line ratio maps, for each spaxel, of the four enlarged reference regions (their exact location in the galaxy disc may be seen in Fig. A3). A detection threshold of  $3\sigma$  on the individual lines was applied to produce the maps. It also presents a plot of the variation of the global line ratios extracted from the integrated spectrum of each region as a function of the galactocentric radius. These plots are color coded according to different SNR thresholds. The best polynomial fit obtained in the case of the highest  $\text{SNR}_{cross}$  subsample is drawn over each plot (and its corresponding equation is written at the top of each plot). The HII regions from the CHAOS project (Berg et al. 2015) are superimposed to the SITELE's regions in the plots of the line ratios.

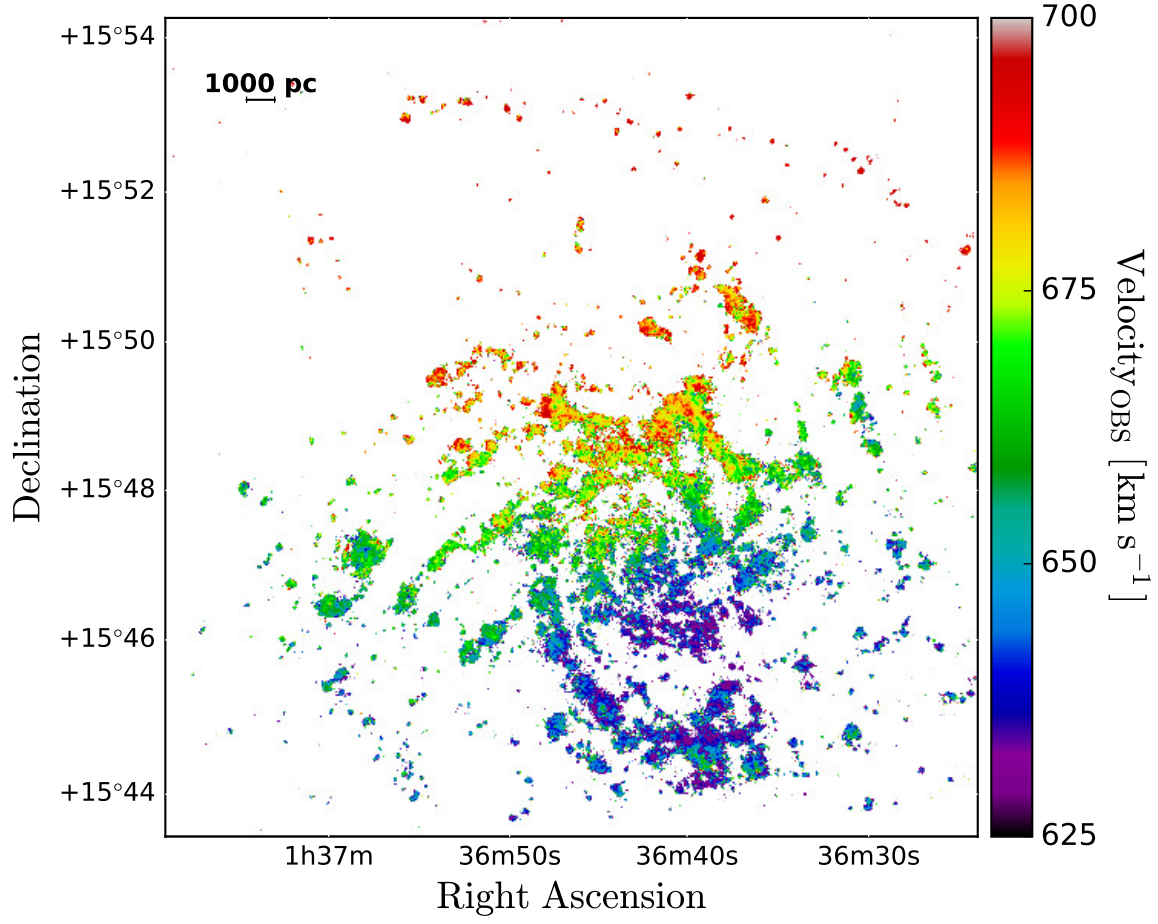


**Figure A1.** The final velocity map of NGC 628 based on the SN3 filter (which includes the strong  $\text{H}\alpha$  emission line). Spaxels with  $\text{SNR}_{\text{H}\alpha} > 3$  have been selected.



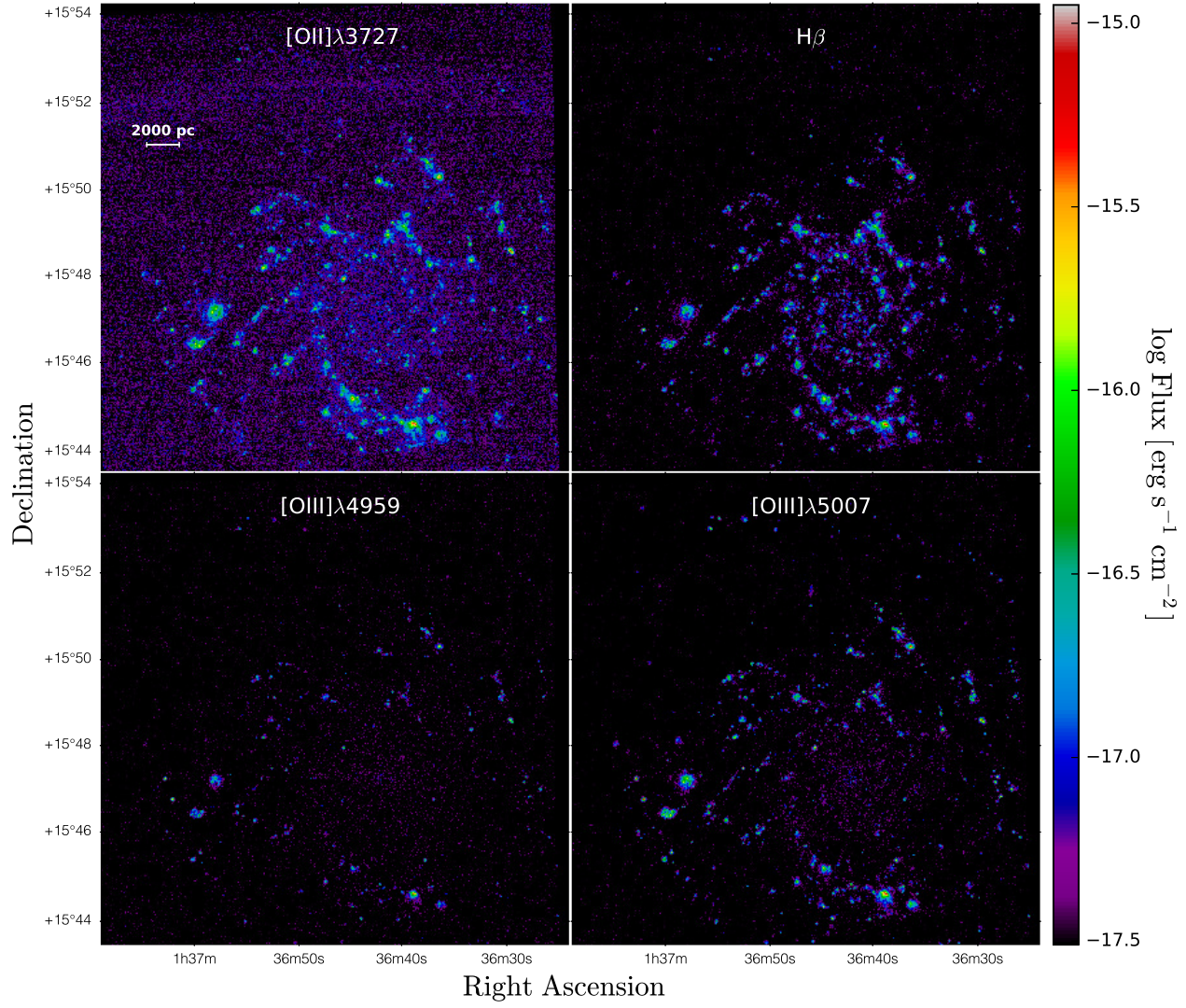


**Figure A2.** Flux map of the emission lines measured in the SN1 and SN2 datacubes. The correction for the internal extinction is not applied.

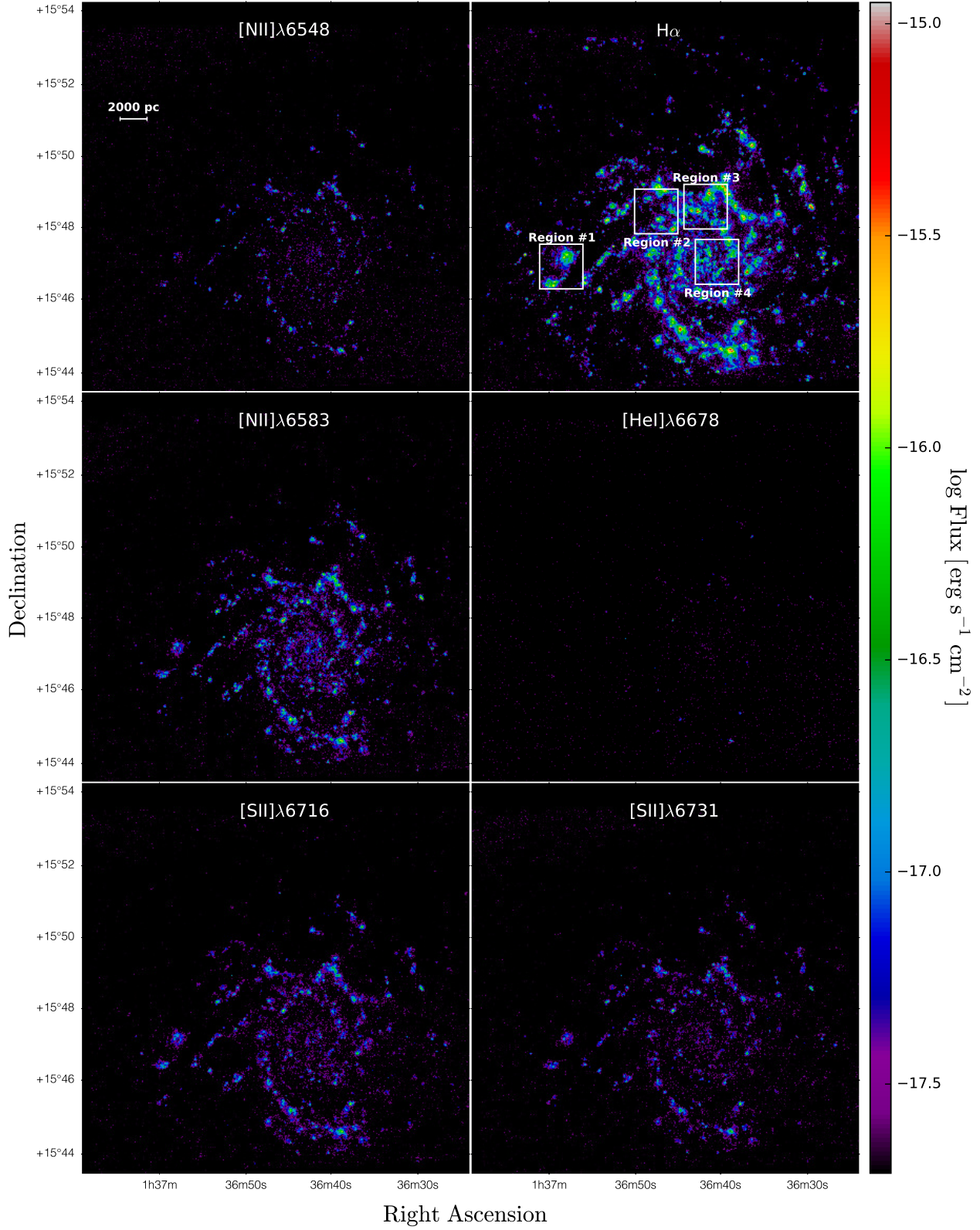


**Figure A3.** Flux map of the emission lines measured in the SN3 datacube. The correction for the internal extinction is not applied.



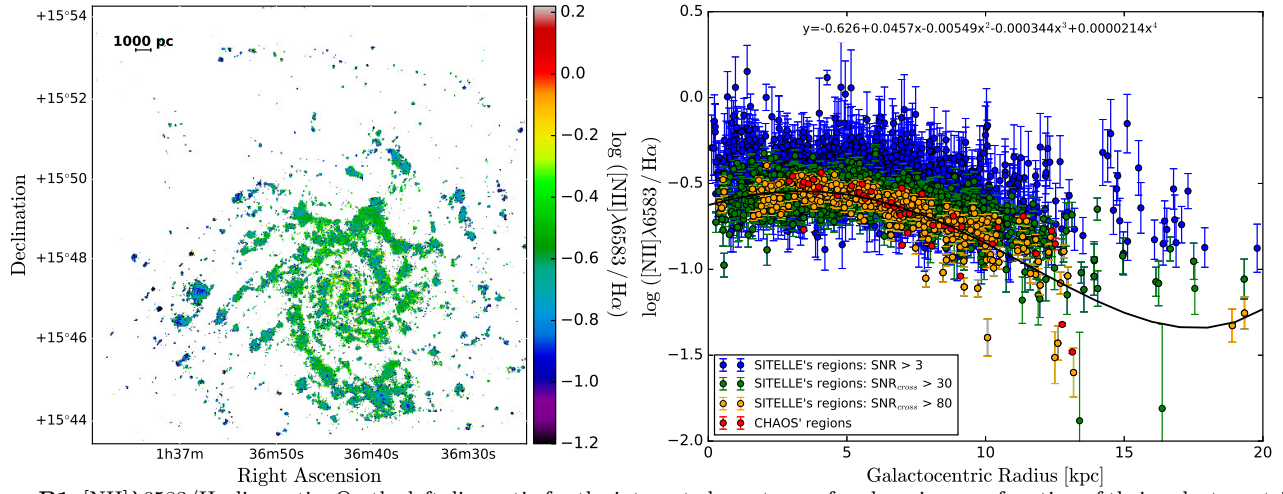


**Figure B1.**  $[\text{NII}]\lambda 6583/\text{H}\alpha$  line ratio. On the left, line ratio for the integrated spectrum of each region as a function of their galactocentric radius. Three thresholds of the SNR have been considered and the CHAOS regions have been superimposed to the SITELLE's data. The black curve is a fit to the highest SNR<sub>cross</sub> subsample of regions.

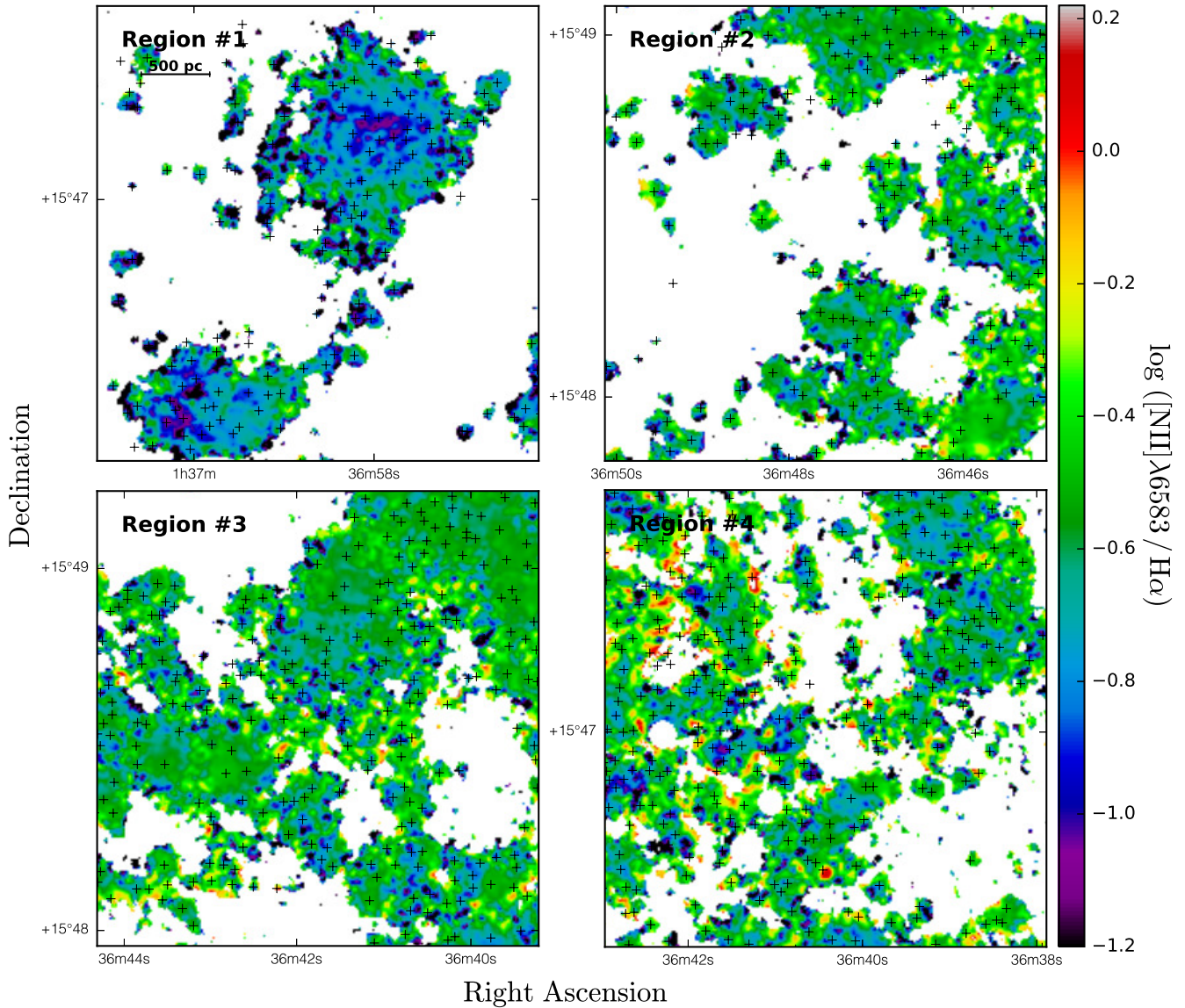


**Figure B2.** Map of the  $[\text{NII}]\lambda 6583/\text{H}\alpha$  line ratio for areas defined in Figure A3. Black crosses indicate the location of the emission peaks (identified in § 4).



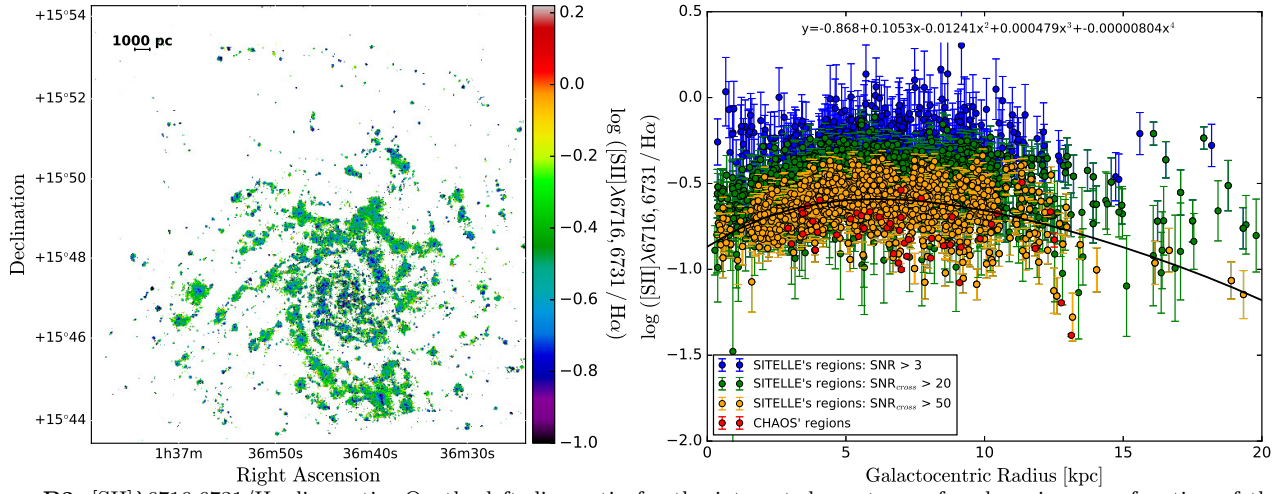


**Figure B3.**  $[SII]\lambda 6716, 6731 / H\alpha$  line ratio. On the left, line ratio for the integrated spectrum of each region as a function of their galactocentric radius. Three thresholds of the SNR have been considered and the CHAOS regions have been superimposed to the SITELLE's data. The black curve is a fit to the highest SNR<sub>cross</sub> subsample of regions.

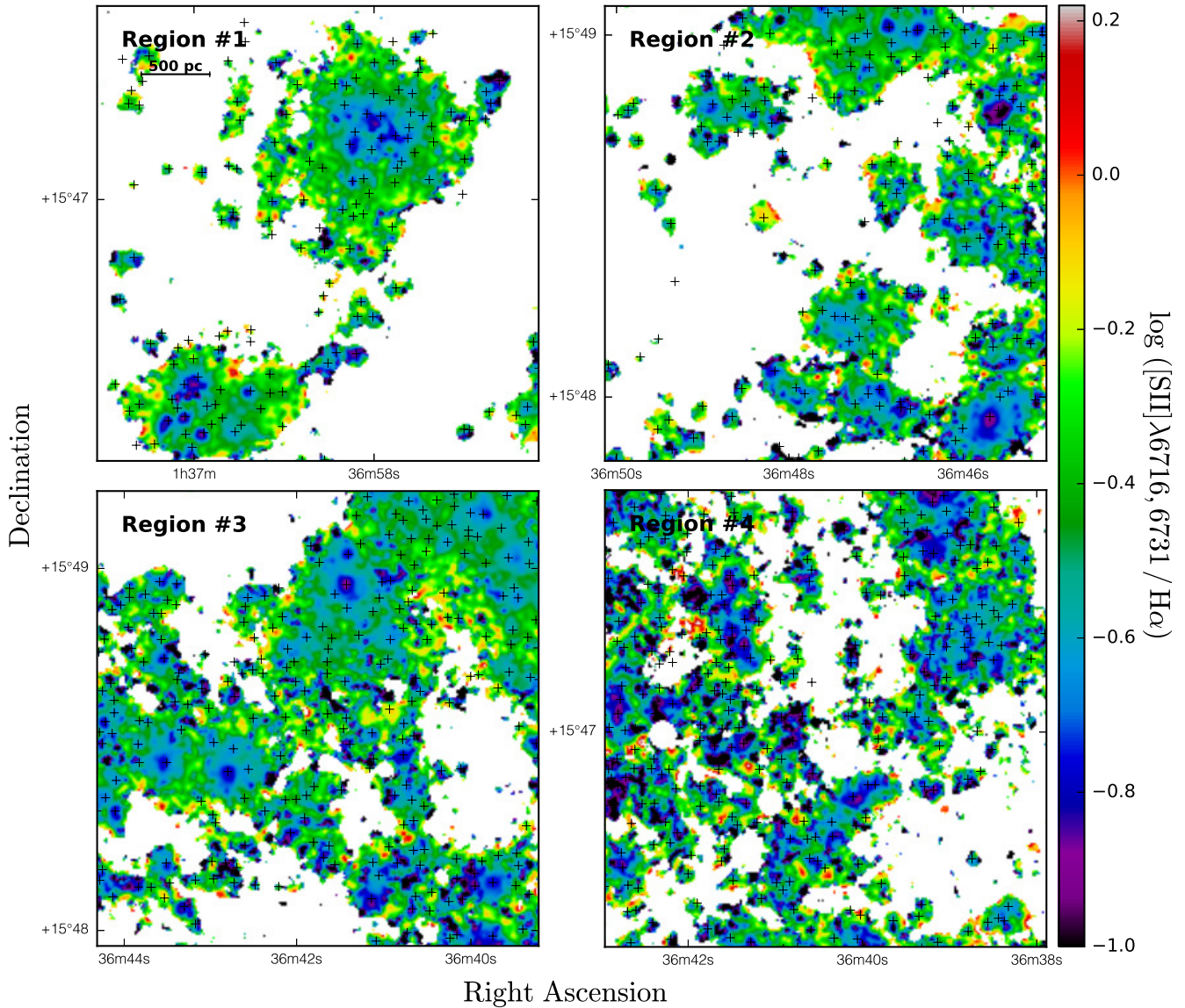


**Figure B4.** Map of the  $[SII]\lambda 6716, 6731 / H\alpha$  line ratio for areas defined in Figure A3. Black crosses indicate the location of the emission peaks (identified in § 4).

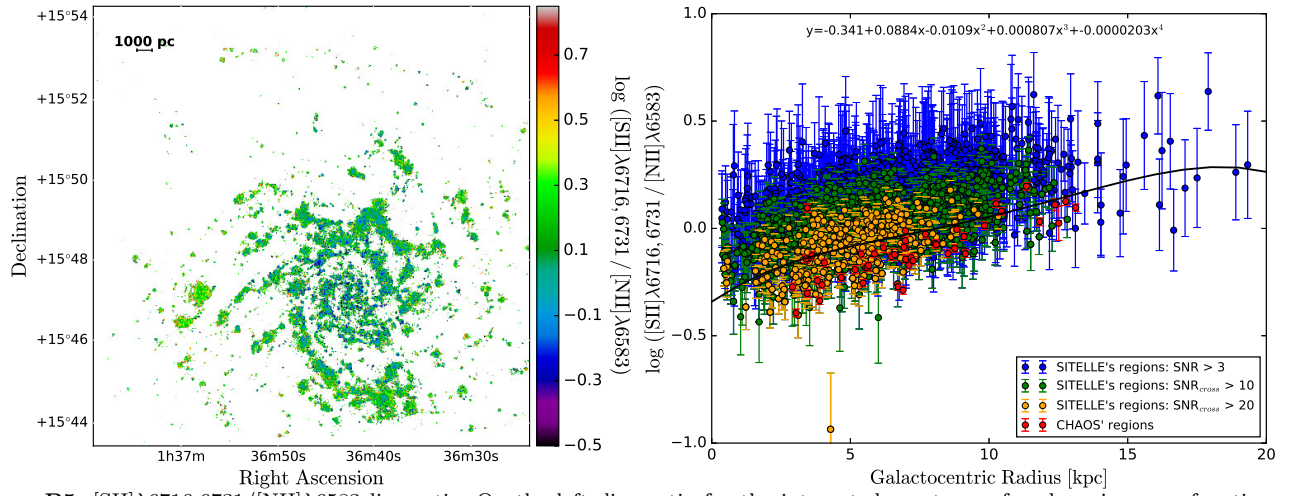


**Figure B5.**  $[\text{SII}]\lambda 6716, 6731 / [\text{NII}]\lambda 6583$  line ratio. On the left, line ratio for the integrated spectrum of each region as a function of their galactocentric radius. Three thresholds of the SNR have been considered and the CHAOS regions have been superimposed to the SITELLE's data. The black curve is a fit to the highest  $\text{SNR}_{\text{cross}}$  subsample of regions.

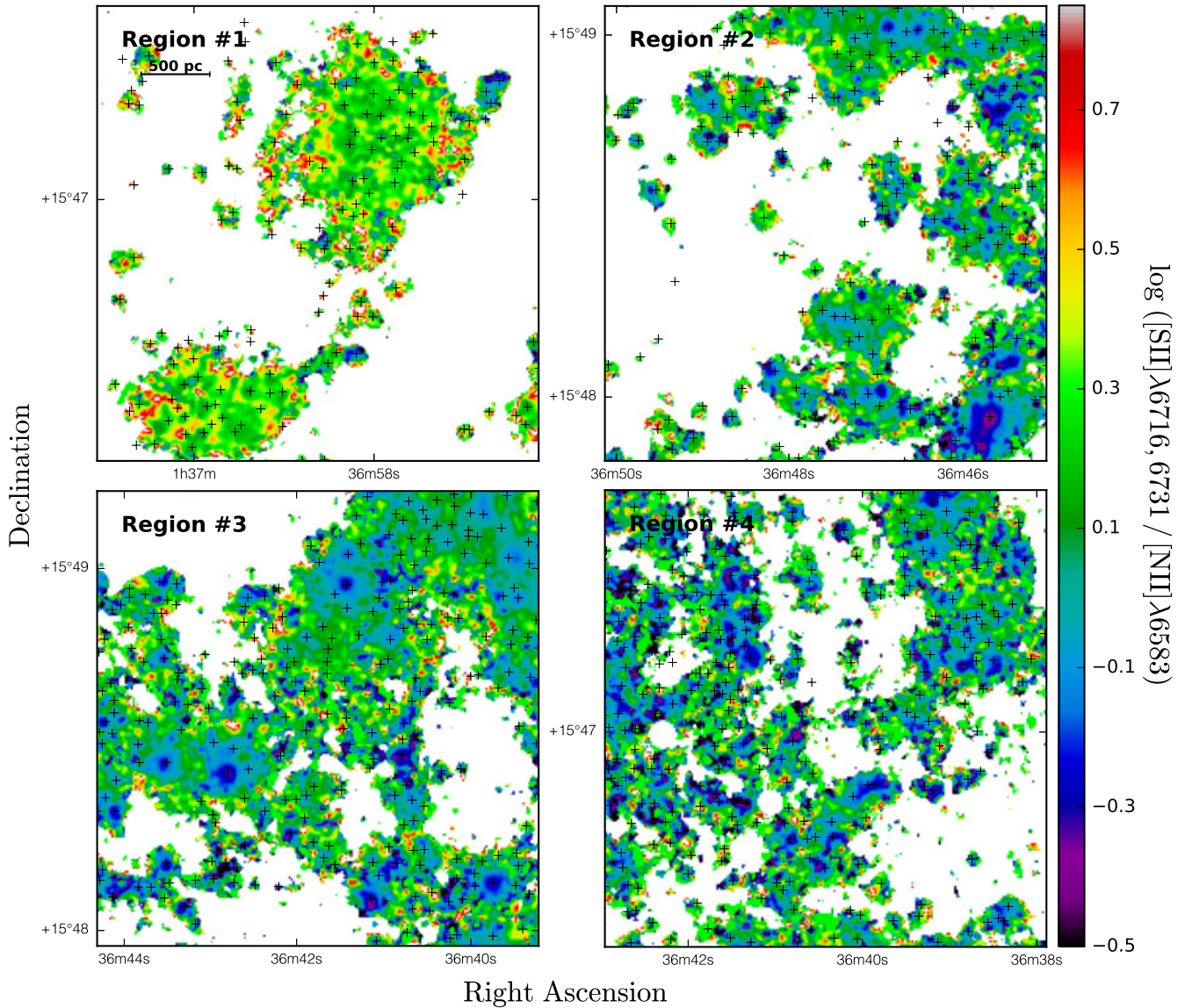


**Figure B6.** Map of the  $[\text{SII}]\lambda 6716, 6731 / [\text{NII}]\lambda 6583$  line ratio for areas defined in Figure A3. Black crosses indicate the location of the emission peaks (identified in § 4).



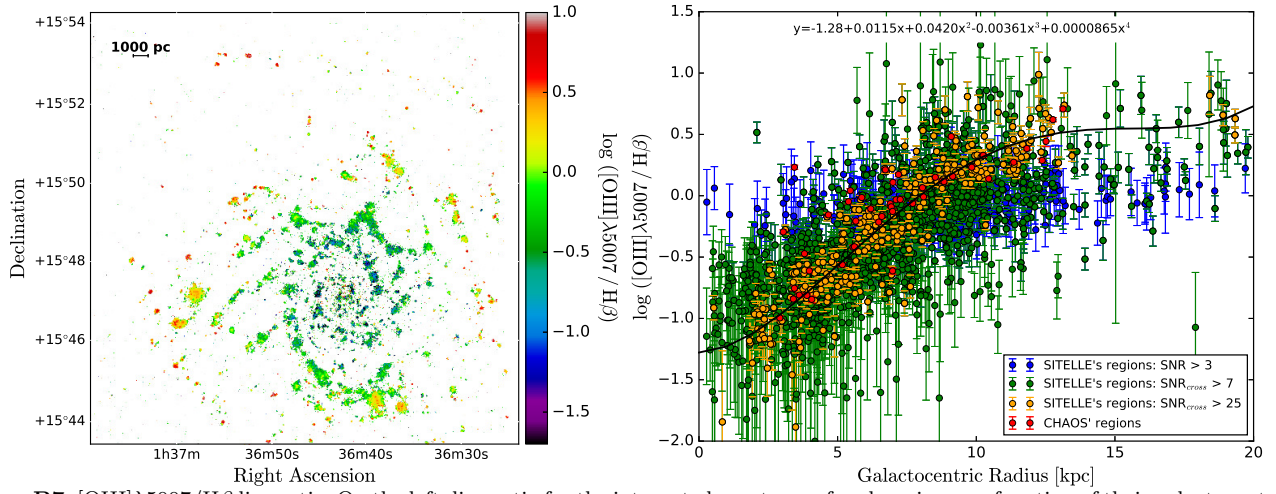


**Figure B7.**  $[\text{OIII}]\lambda 5007/\text{H}\beta$  line ratio. On the left, line ratio for the integrated spectrum of each region as a function of their galactocentric radius. Three thresholds of the SNR have been considered and the CHAOS regions have been superimposed to the SITELLE's data. The black curve is a fit to the highest  $\text{SNR}_{\text{cross}}$  subsample of regions.

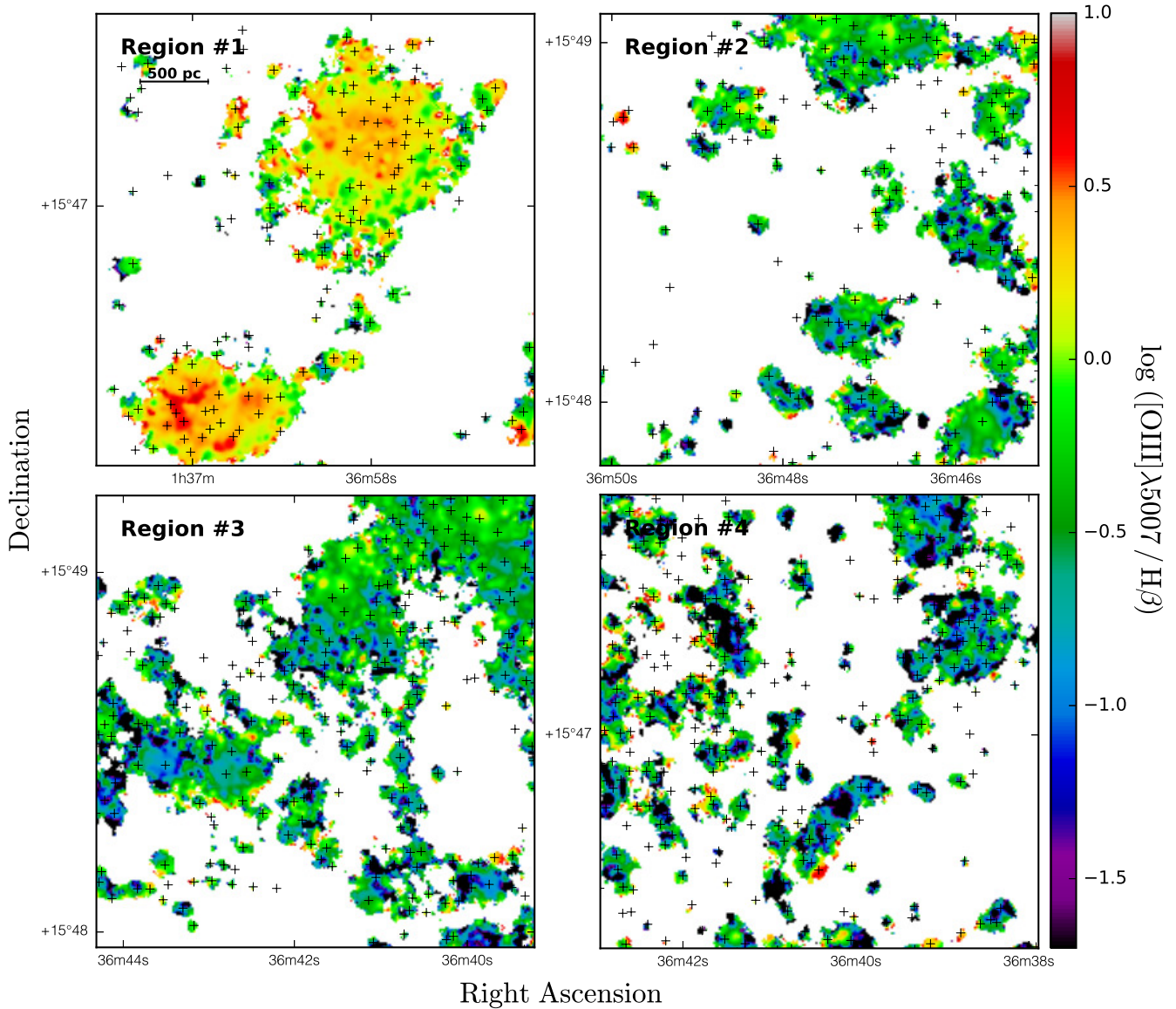


**Figure B8.** Map of the  $[\text{OIII}]\lambda 5007/\text{H}\beta$  line ratio for areas defined in Figure A3. Black crosses indicate the location of the emission peaks (identified in § 4).

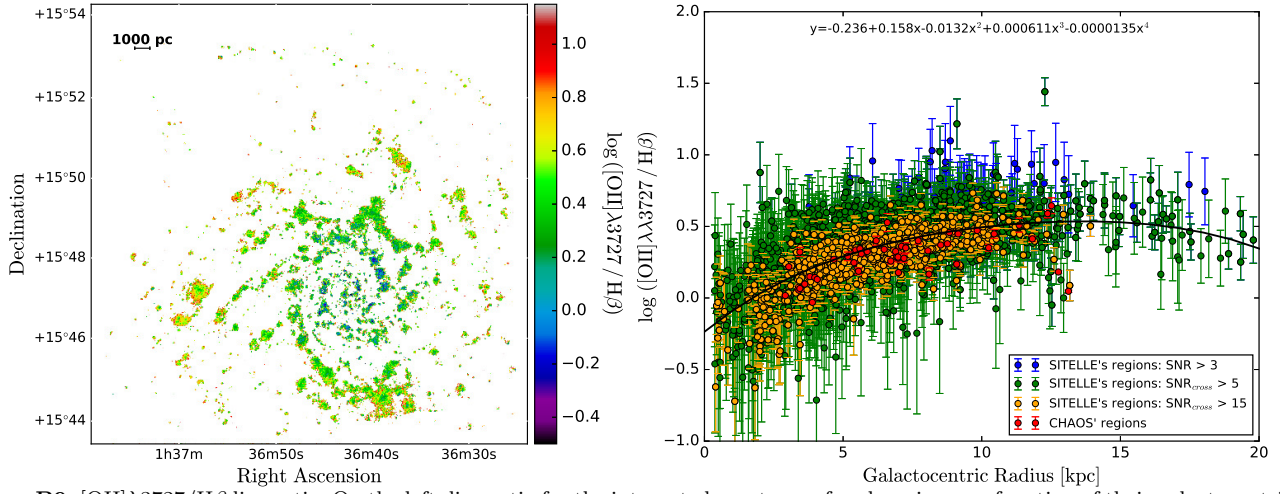


**Figure B9.**  $[\text{OII}]\lambda 3727/\text{H}\beta$  line ratio. On the left, line ratio for the integrated spectrum of each region as a function of their galactocentric radius. Three thresholds of the SNR have been considered and the CHAOS regions have been superimposed to the SITELLE's data. The black curve is a fit to the highest  $\text{SNR}_{\text{cross}}$  subsample of regions.

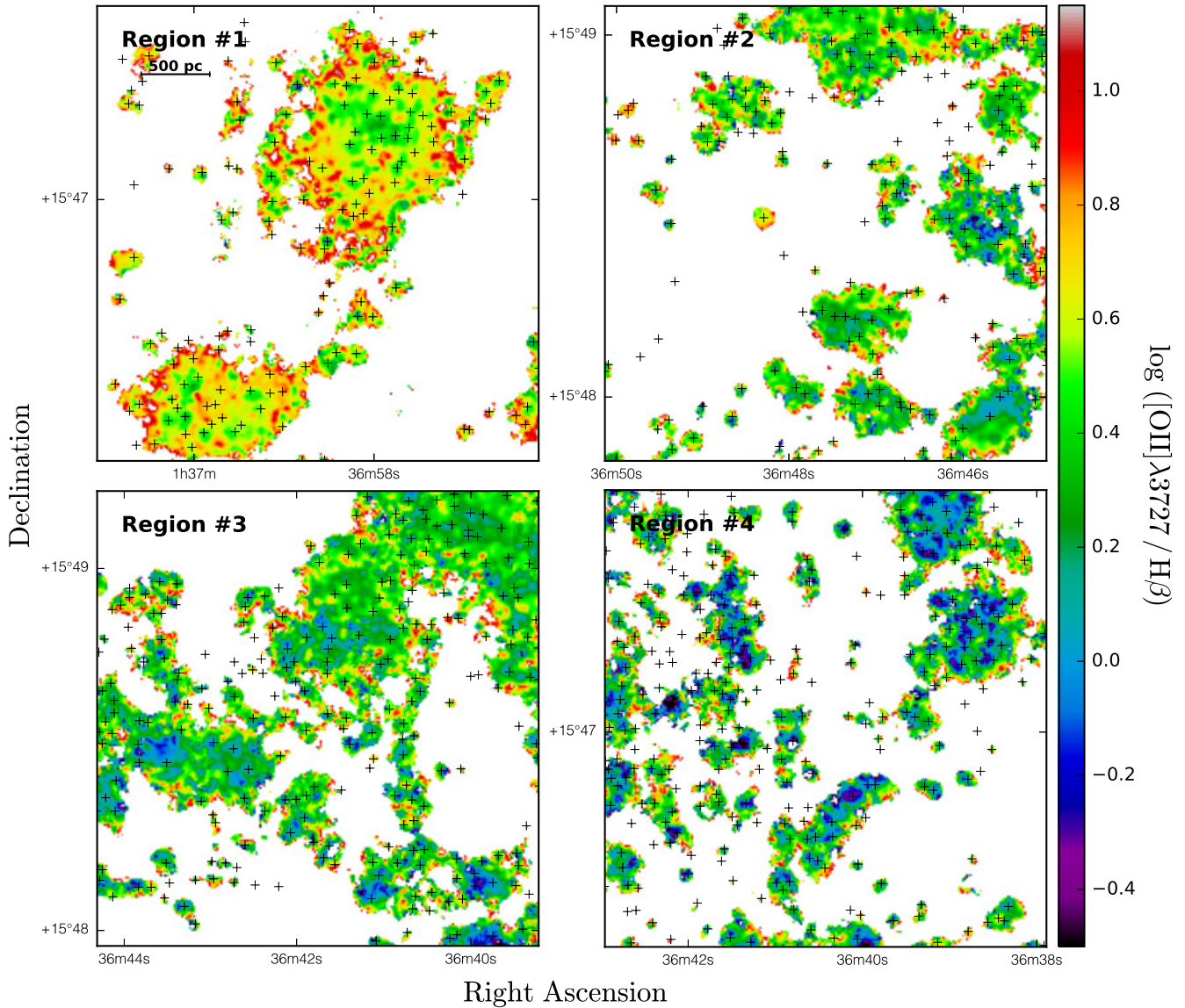


**Figure B10.** Map of the  $[\text{OII}]\lambda 3727/\text{H}\beta$  line ratio for areas defined in Figure A3. Black crosses indicate the location of the emission peaks (identified in § 4).



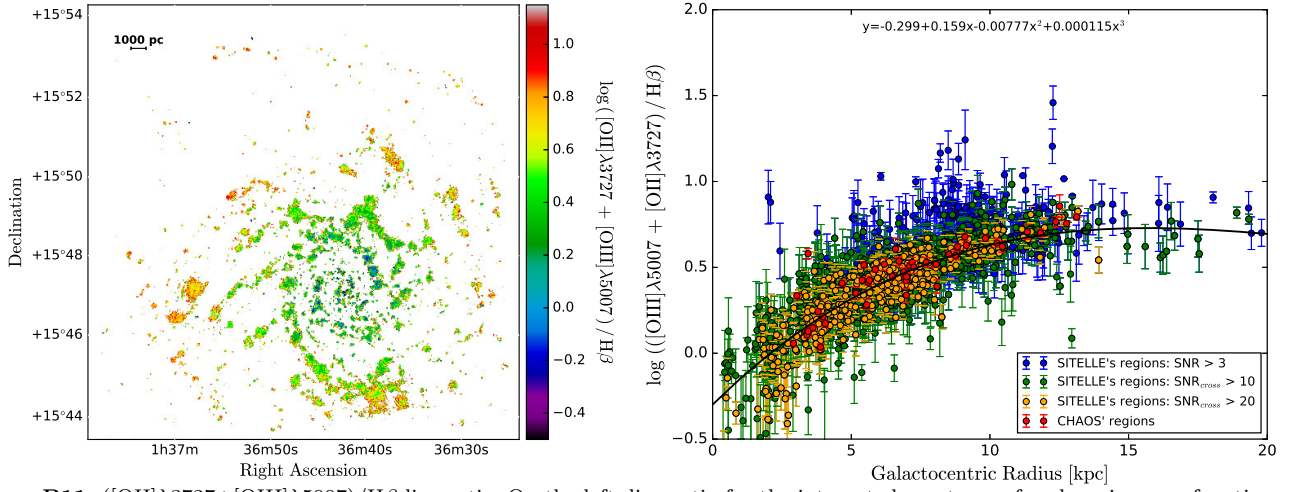


**Figure B11.**  $([\text{OII}]\lambda 3727 + [\text{OIII}]\lambda 5007)/\text{H}\beta$  line ratio. On the left, line ratio for the integrated spectrum of each region as a function of their galactocentric radius. Three thresholds of the SNR have been considered and the CHAOS regions have been superimposed to the SITELLE's data. The black curve is a fit to the highest  $\text{SNR}_{\text{cross}}$  subsample of regions.

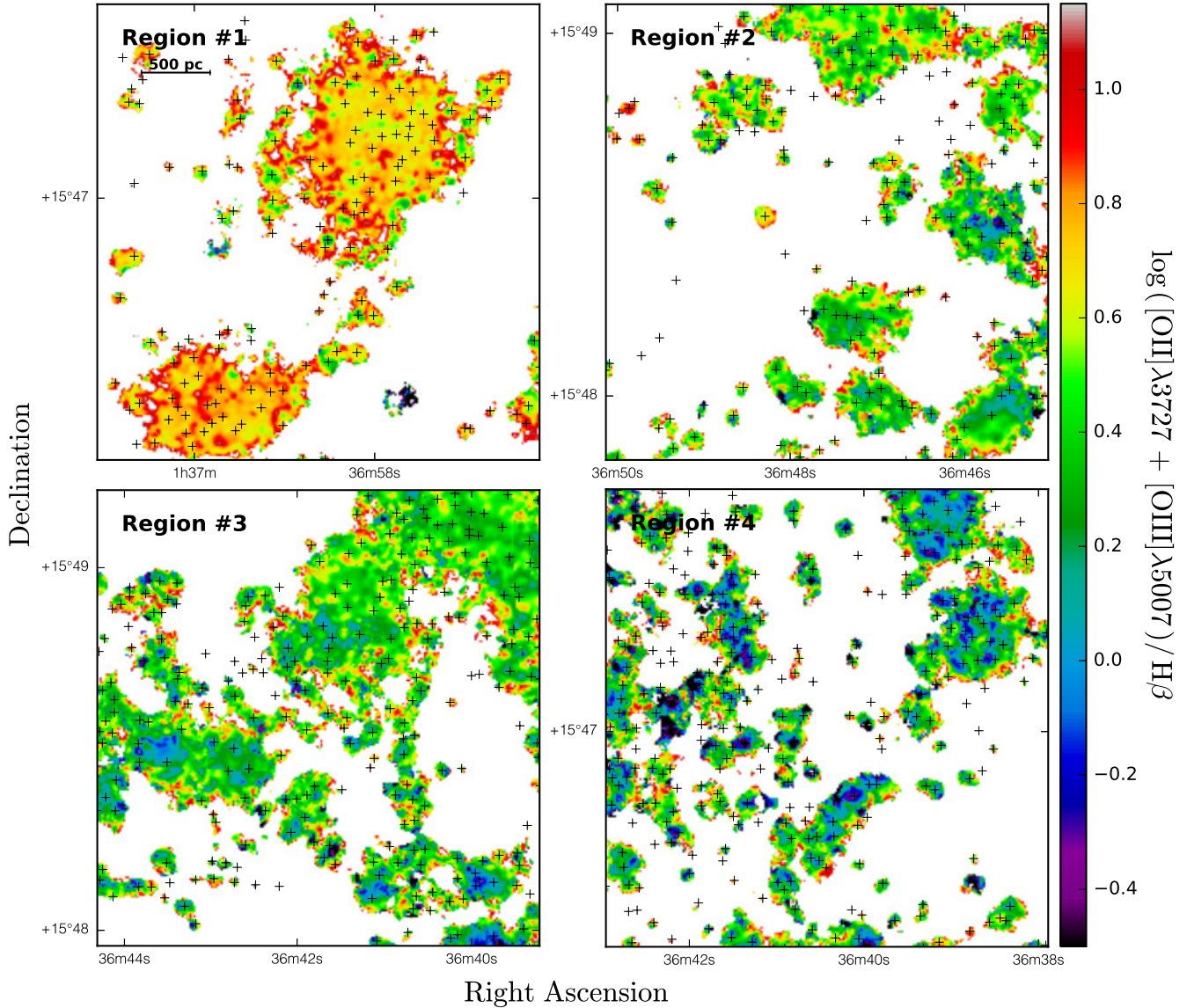


**Figure B12.** Map of the  $([\text{OII}]\lambda 3727 + [\text{OIII}]\lambda 5007)/\text{H}\beta$  line ratio for areas defined in Figure A3. Black crosses indicate the location of the emission peaks (identified in § 4).

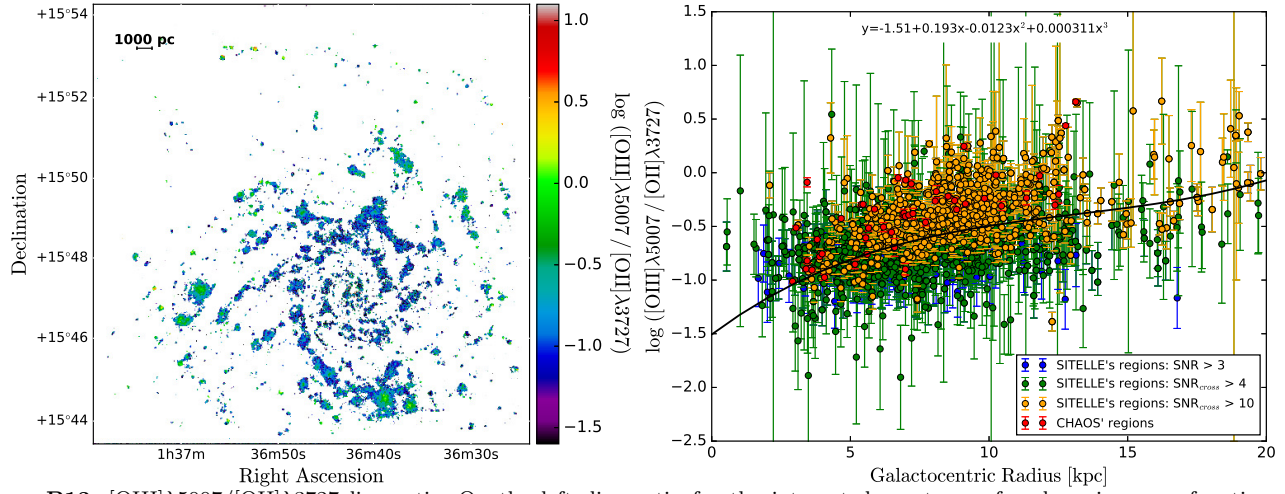


**Figure B13.**  $[\text{OIII}]\lambda 5007/[\text{OII}]\lambda 3727$  line ratio. On the left, line ratio for the integrated spectrum of each region as a function of their galactocentric radius. Three thresholds of the SNR have been considered and the CHAOS regions have been superimposed to the SITELLE's data. The black curve is a fit to the highest  $\text{SNR}_{\text{cross}}$  subsample of regions.

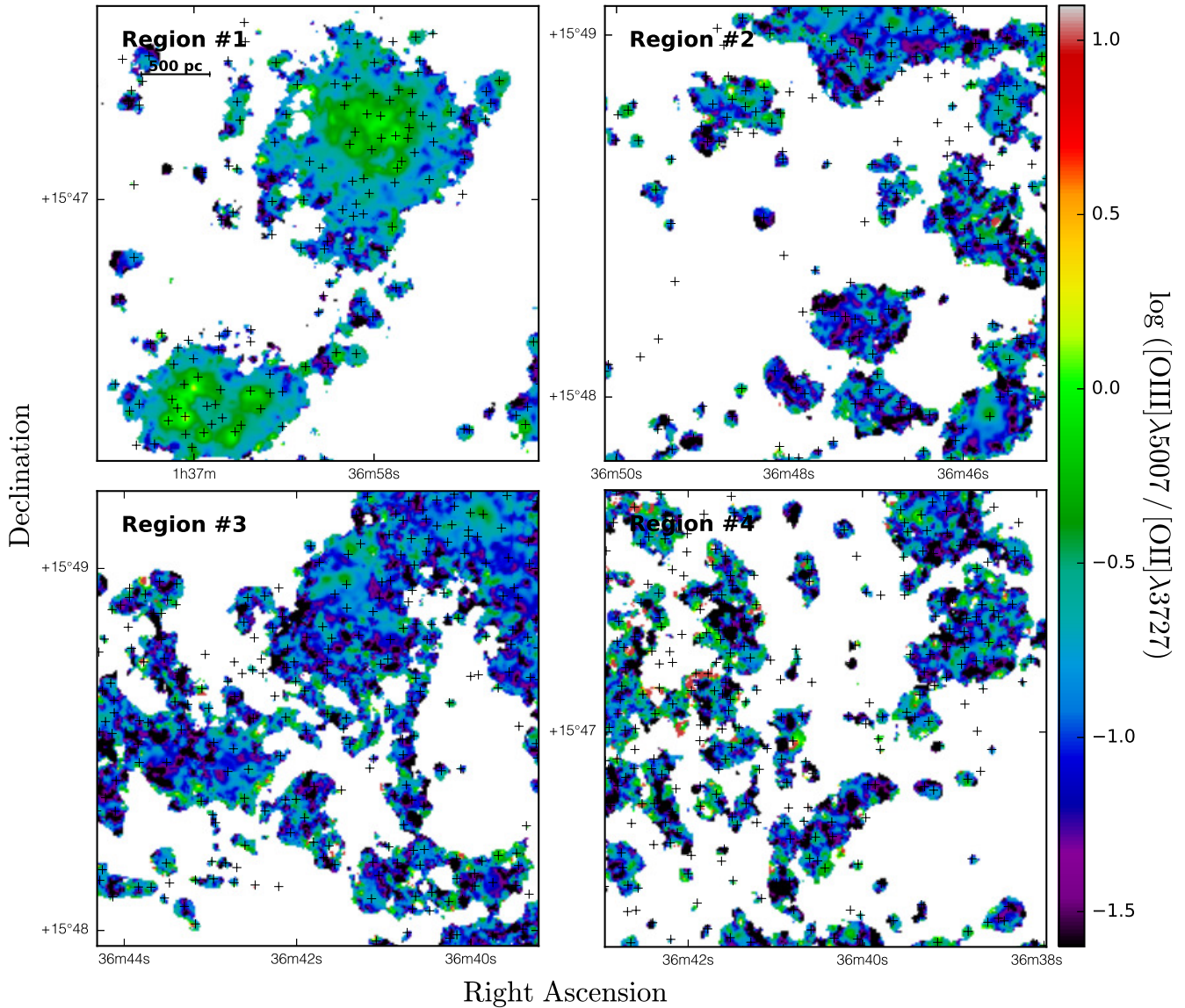


**Figure B14.** Map of the  $[\text{OIII}]\lambda 5007/[\text{OII}]\lambda 3727$  line ratio for areas defined in Figure A3. Black crosses indicate the location of the emission peaks (identified in § 4).



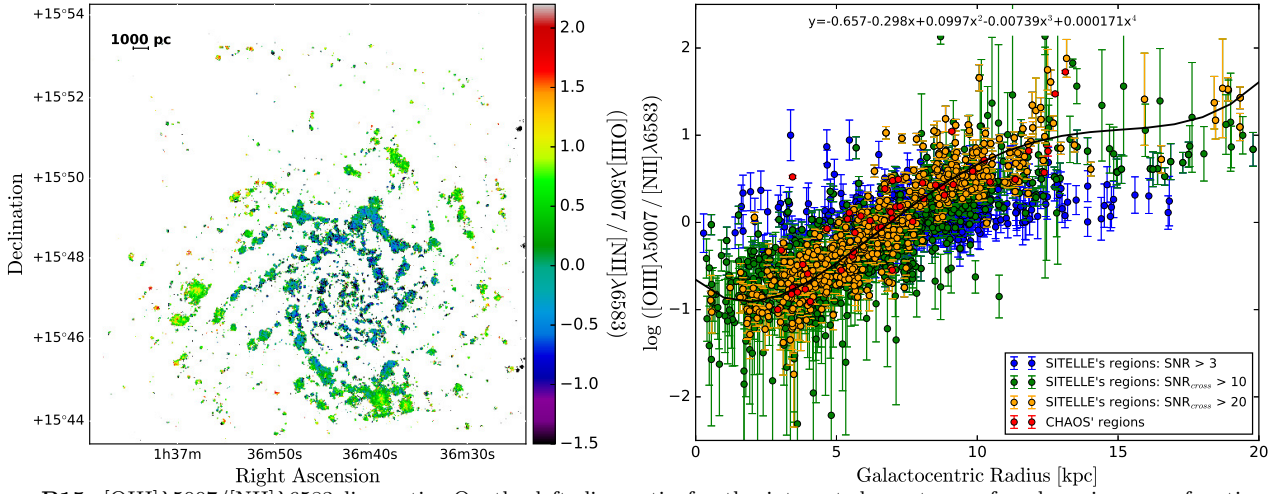


**Figure B15.**  $[\text{OIII}]\lambda 5007/[\text{NII}]\lambda 6583$  line ratio. On the left, line ratio for the integrated spectrum of each region as a function of their galactocentric radius. Three thresholds of the SNR have been considered and the CHAOS regions have been superimposed to the SITELLE's data. The black curve is a fit to the highest  $\text{SNR}_{\text{cross}}$  subsample of regions.

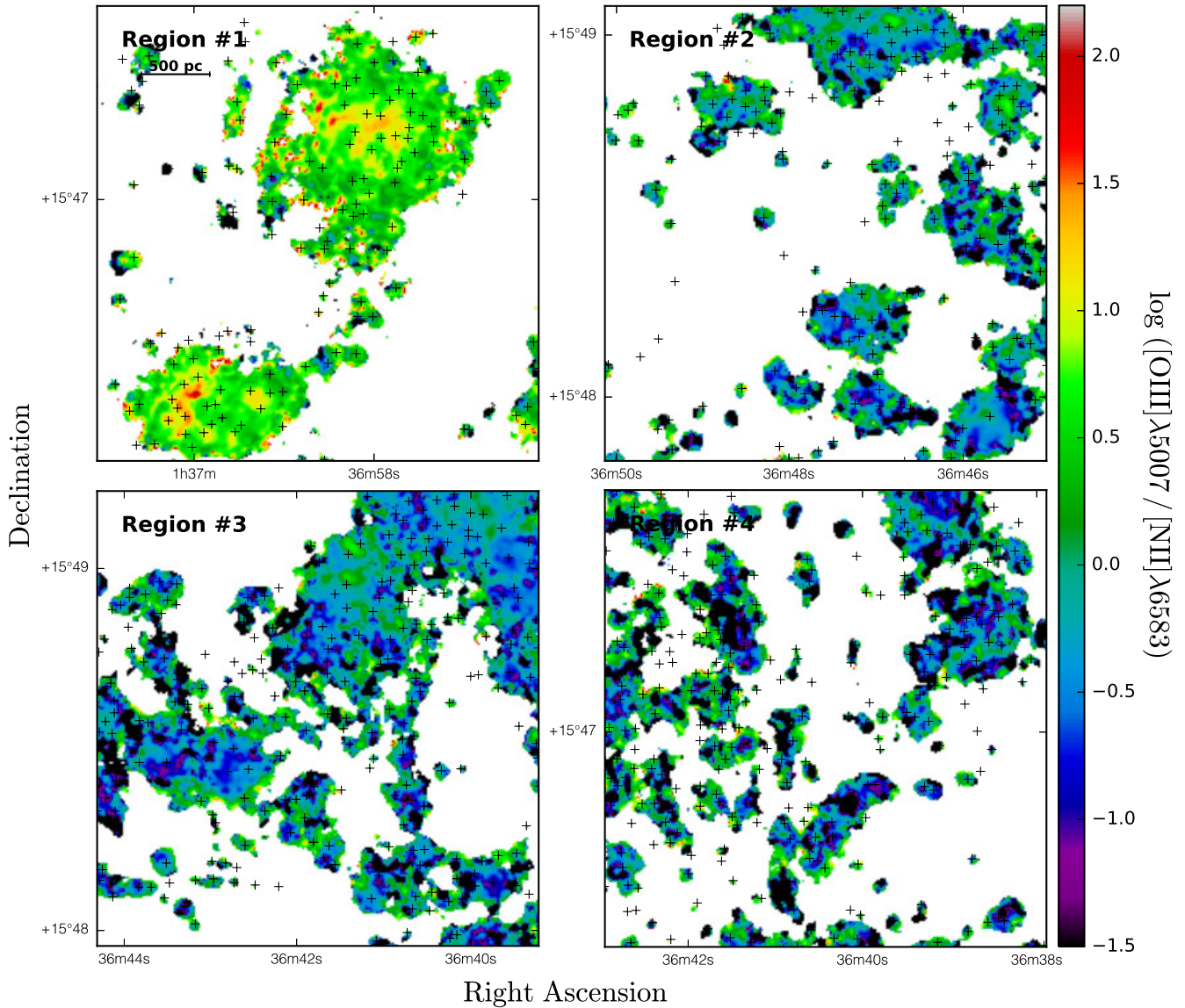


**Figure B16.** Map of the  $[\text{OIII}]\lambda 5007/[\text{NII}]\lambda 6583$  line ratio for areas defined in Figure A3. Black crosses indicate the location of the emission peaks (identified in § 4).



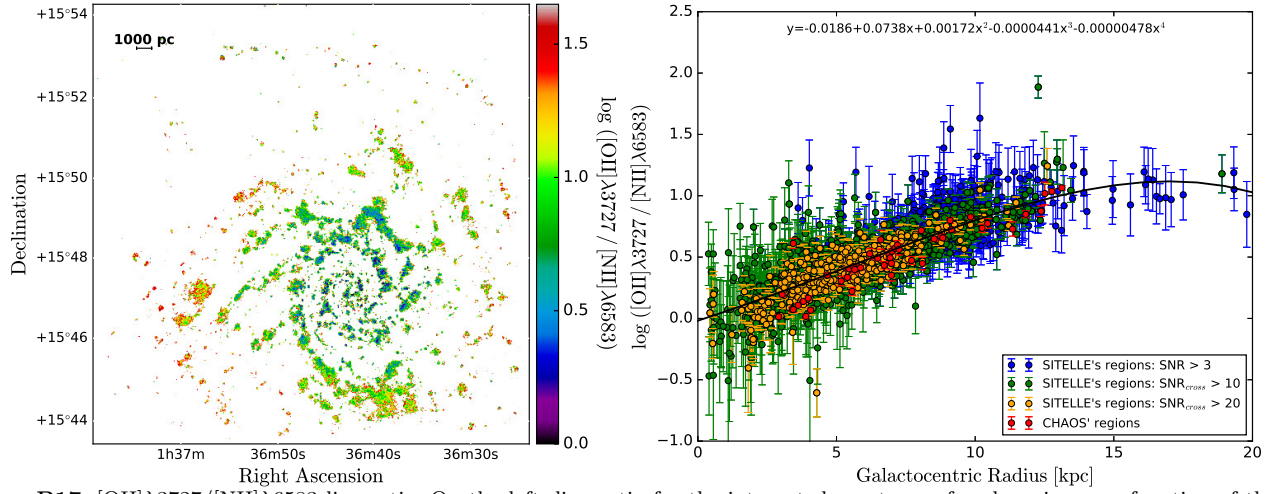


**Figure B17.**  $[\text{OII}]\lambda 3727/[\text{NII}]\lambda 6583$  line ratio. On the left, line ratio for the integrated spectrum of each region as a function of their galactocentric radius. Three thresholds of the SNR have been considered and the CHAOS regions have been superimposed to the SITELLE's data. The black curve is a fit to the highest  $\text{SNR}_{\text{cross}}$  subsample of regions.

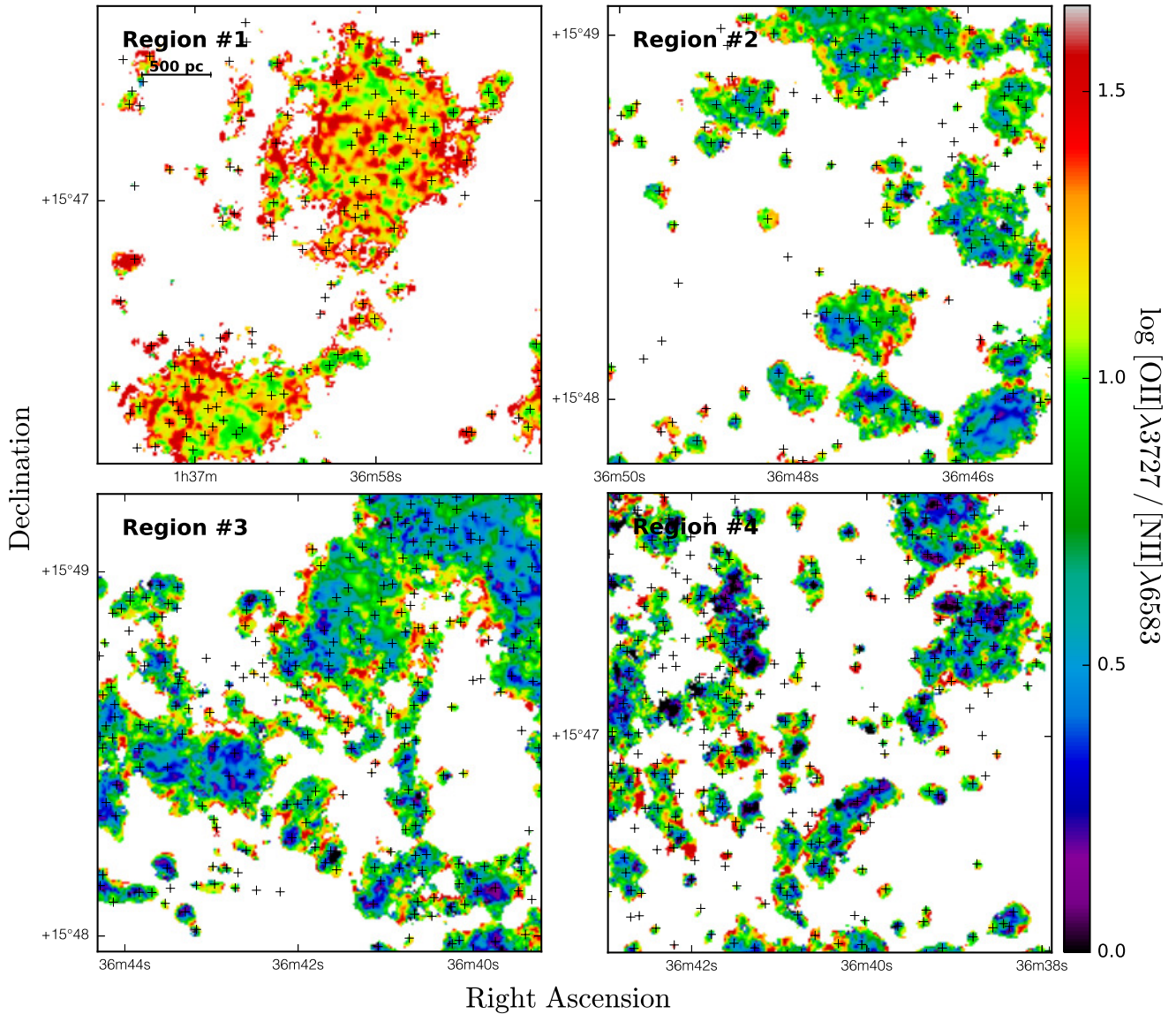


**Figure B18.** Map of the  $[\text{OII}]\lambda 3727/[\text{NII}]\lambda 6583$  line ratio for areas defined in Figure A3. Black crosses indicate the location of the emission peaks (identified in § 4).

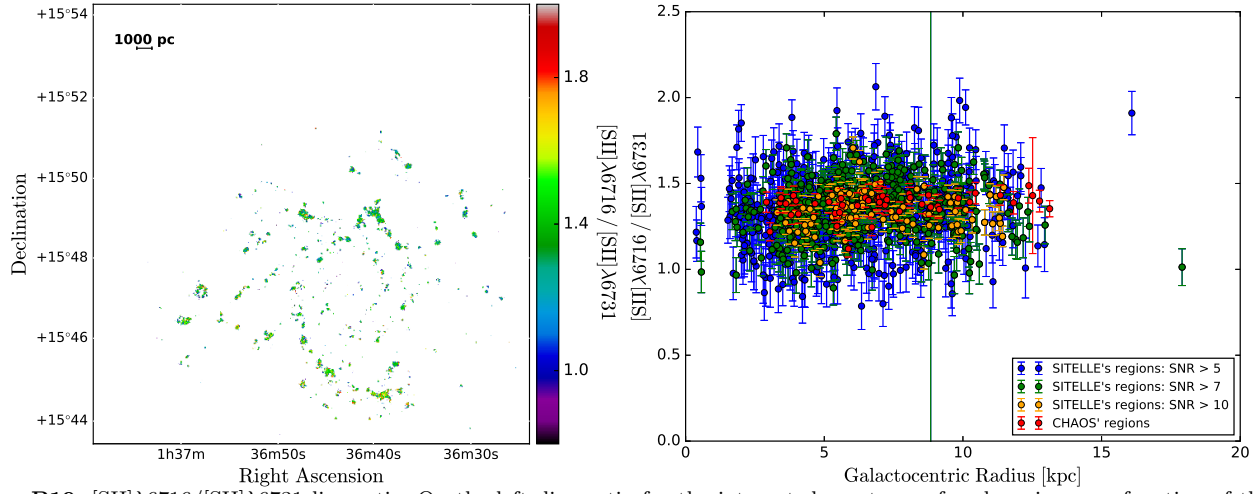


**Figure B19.**  $[\text{SII}]\lambda 6716 / [\text{SII}]\lambda 6731$  line ratio. On the left, line ratio for the integrated spectrum of each region as a function of their galactocentric radius. Three thresholds of the SNR have been considered and the CHAOS regions have been superimposed to the SITELLE's data.

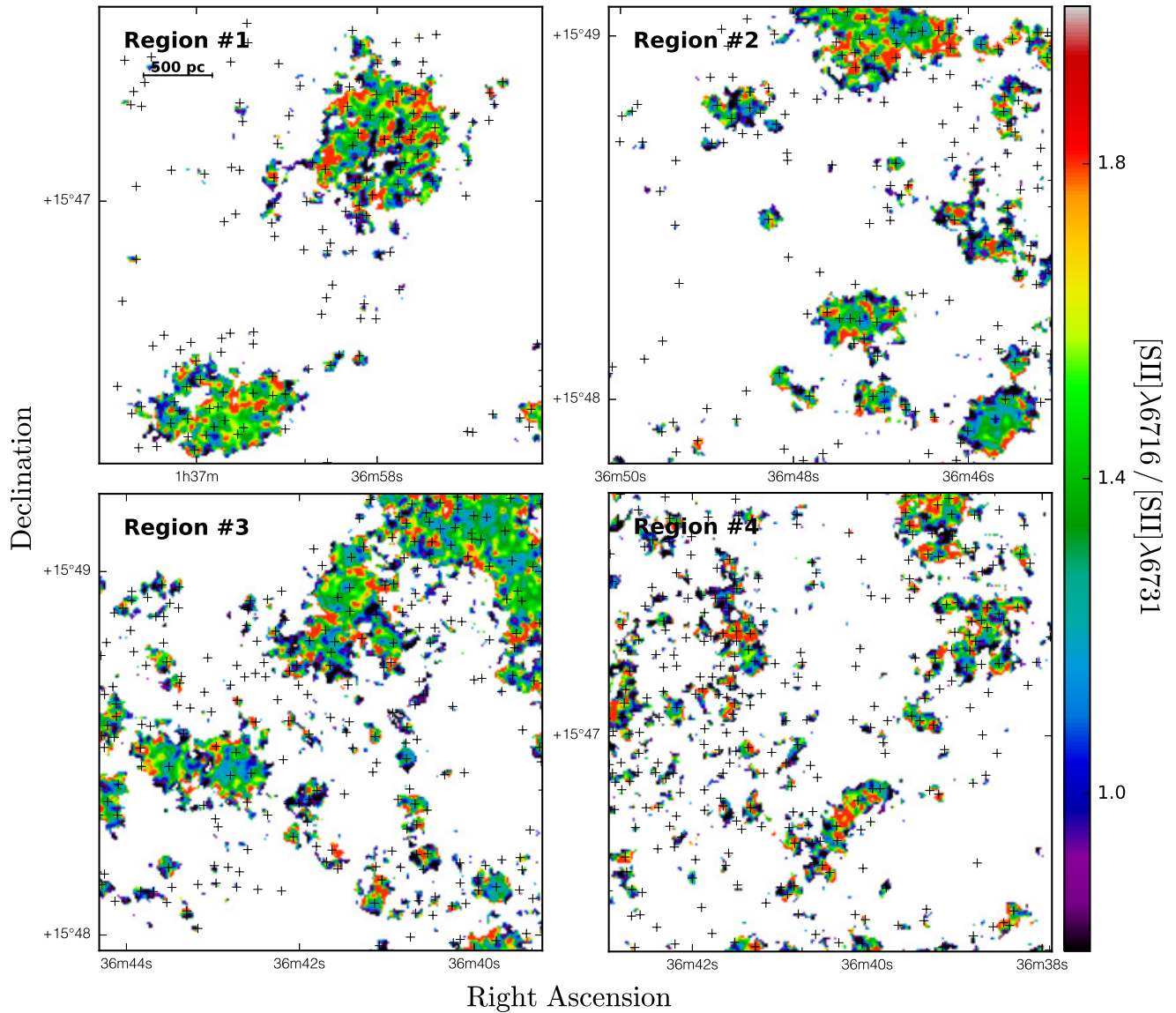


**Figure B20.** Map of the  $[\text{SII}]\lambda 6716 / [\text{SII}]\lambda 6731$  line ratio for areas defined in Figure A3. Black crosses indicate the location of the emission peaks (identified in § 4).